Probing the positron phase of a Thermonuclear Supernova

Jan Lindahl

November 12, 2003

Abstract

The Type Ia thermonuclear supernova SN 2000cx has been observed at phases between 360 to 480 days past maximum light. The observations were conducted at the Very Large Telescope (VLT) in the optical UBVRI bands and in the near–infrared JHK bands. SN 2000cx was the brightest SN that year and positioned far from the nucleus of its host galaxy NGC 524, so it could be followed up to late times. This is the first time observations have been done in both optical and near–infrared wavelengths at late times. Little near–infrared observations at these late phases exist previous. At these late times the positrons from the radioactive decay of ^{56}Co to ^{56}Fe are the dominating energy source that powers the light curve. Previous studies show that the observed light curve falls more steeply than predicted. This has been interpreted as due to positron escape from the ejecta. The assumption made here is that the "bolometric" (UVOIR) light curve behaves in the same way as the V band light curve.

Our new observations show a decline in all of the optical passbands but in the near–infrared we get constant magnitudes for the different passbands. With our observations for four different epochs in the optical wavelengths, and with three epochs in the near–infrared wavelengths, we can construct a bolometric light curve. We show that the V band does not follow the bolometric light curve, and it deviates from it with time. The interpretation of positron escape could instead be explained by a temperature effect, when more of the emission is emitted at near–infrared wavelengths.

This is a 20 p master thesis by Jan Lindahl conducted at Stockholm Observatory during the period 2002–2003. I would like to thank my supervisor Jesper Sollerman for helpful discussion and suggestions. I would also like to thank the rest of the staff at the observatory that has made this work possible.

Contents

List of Figures

List of Tables

1 Introduction

A supernova is an exploding star. They can become almost as bright as the entire galaxy where they exist. Since there are billions of stars in a galaxy, yet altogether they are emitting almost as much light as the single brilliant star. Supernovae represent the end point of normal stellar evolution, so by studying them and the evolutionary pathways that lead to them, we can gain insights into the whole course of stellar evolution. In the evolution and subsequent explosion, supernovae forge the majority of the heavy elements and hence drive the chemical evolution of the galaxies. In addition, the energetic input of supernovae may influence the birth of new stars by compressing interstellar gas. Because supernovae are so bright they can be observed at great distances and can serve as distance indicators to measure the very scale of the universe. The kinetic energy of the explosion is of the order 10^{51} ergs, and the velocity of the ejected material is about a hundredth of the speed of light.

1.1 History

Several supernovae are described in the ancient literature. In China they observed the star which exploded in 1054, and which is now known as the Crab nebula. Other famous supernovae are the ones observed by Tycho in 1572 and Kepler in 1604. Keplers supernova is the last one observed in our galaxy. So how often does these events happens? Are they rare events or are they fairly common? It is estimated that our galaxy experiences one supernova every 40 years (Tamman 1982). The supernova that appeared 1885 in the Andromeda Galaxy was the first one which was observed spectroscopically, because the technique was not developed before that time. About 50 years later the Swiss astronomer Fritz Zwicky and the German-American astronomer Walter Baade proposed the name supernovae (Zwicky & Baade 1934). Zwicky also proposed that special observing patrols must be organized to look for supernovae. The idea was that by systematically monitoring many hundreds of galaxies we might hope to observe one or two supernovae annually. The first supernova patrol was instituted in 1933 by Zwicky, using a very modest 10–inch telescope. During the period 1936 – 1939 he observed 12 supernovae in different galaxies. The supernovae discovered were investigated both photometrically and spectroscopically. Light curves as well as spectra were obtained for these supernovae (see Shklovskii 1978). The spectra of one type were similar from event to event. Their light curves (luminosity as a function of time) had a predictable regularity. They rose to peak brightness in about two weeks and then after declining for two more weeks, they faded in an almost exponential fashion. Other events were dimmer at maximum by a factor of a few in luminosity and had light curves which rose and faded in a manner that varied from supernova to supernova. The most important aspect of these events, which differentiated them as a separate class, was that their spectra contained the common optical lines of hydrogen. These two different kinds of supernova were differentiated by Minkowski (1941) as Type I and Type II, respectively.

Type I are today sub classified according to features of their spectra:

- SN Ia (Si)
- SN Ib (no Si, He)
- SN Ic (no Si, no He)

Type Ib and Type Ic supernovae are believed to be the result of core collapse of massive stars that has lost their hydrogen envelope before explosion (Höflich 1999). The Type II supernovae are also thought to be core collapsing stars.

For the rest of this thesis we are only concidering the Type Ia supernovae.

Type Ia supernova (see Filippenko 1997) have early–time spectra that show lines of neutral and singly ionized intermediate–mass elements such as O, Mg, Si, S, and Ca, with some contribution from iron–peak elements in the near–UV such as Fe and Co. The strongest features are Si II λ6355 and Ca $\lambda\lambda$3934, 3968. After about two weeks the spectra are dominated by lines of Fe II, and after a month the spectra are dominated by forbidden emission lines of Fe and Co (most prominent at ~5900 Å). The cobalt lines decreases with time as the radioactive decay of ^{56}Co.

Supernovae Type Ia are seen in all types of galaxies. In spirals, they also tend to lie between spiral arms or in the halo where we find the older stars. They do not show any evidence of hydrogen in their spectra. Therefor, the progenitors of Type Ia supernovae are believed to be white dwarfs composed of carbon and oxygen, near the Chandrasekhar mass. They accrete material from a close binary companion, reaching M_{CH} and explodes when the burning of carbon triggers the runaway. The companion can be a normal star, which is called a single degenerate scenario, or it could be another white dwarf called the double degenerate scenario.

1.2 Roche lobe overflow

If we consider a binary system where the stars are close to each other, we can take the gravitational field close to each star as circular equipotentials dominated by the 1/r term. Further out the gravitational contributions from the companion star becomes important and the equipotentials will no longer be circular but have a shape of a teardrop. The tips of the teardrops finally merge at a point called the Lagrangian point, and its associated equipotential surface, the Roche lobe (see figure 1).

At far distances the equipotentials again becomes circular because the two stars begin to behave gravitationally like a single point mass. If a particle at the Lagrangian point is given a small outward velocity, it will fall toward the companion star, and if a star gets larger than the Roche lobe surface it begins to lose mass to its companion. If the mass transfer rate is large enough then an accretion disk will form around the other star.

1.3 White Dwarfs

The white dwarfs are stars that are in the end point of their stellar lifes. The nuclear reactions have completely ceased and they can not support themselves against gravity by thermal gas pressure. Instead, the pressure against gravity is supported by the pressure of a degenerate gas. White dwarfs have a typical mass of about 0.7 $M_\odot$ and a radius as that of the Earth. Unlike a normal star, the radius of a degenerate star decreases as the mass increases, and the radius is inversely proportional to the cube root of the mass. The perfect gas law does not apply at these very high densities. When the density inside a star exceeds 10^7 kg/m^3, the electrons become degenerate and their pressure is that of a degenerate gas. The expression for the pressure is $P = h^2/m_e(\mu_e m_H)^{-5/3}\rho^{5/3}$, where h is Planck's constant, m_e is the electron mass, m_H is the hydrogen mass, and μ_e is the mean molecular weight per free electron. Note that the pressure no longer depends on the temperature. Matter in a degenerate state is so tightly squeezed together that atoms are as close together as they can possibly be, and the electrons begin to repel each other.

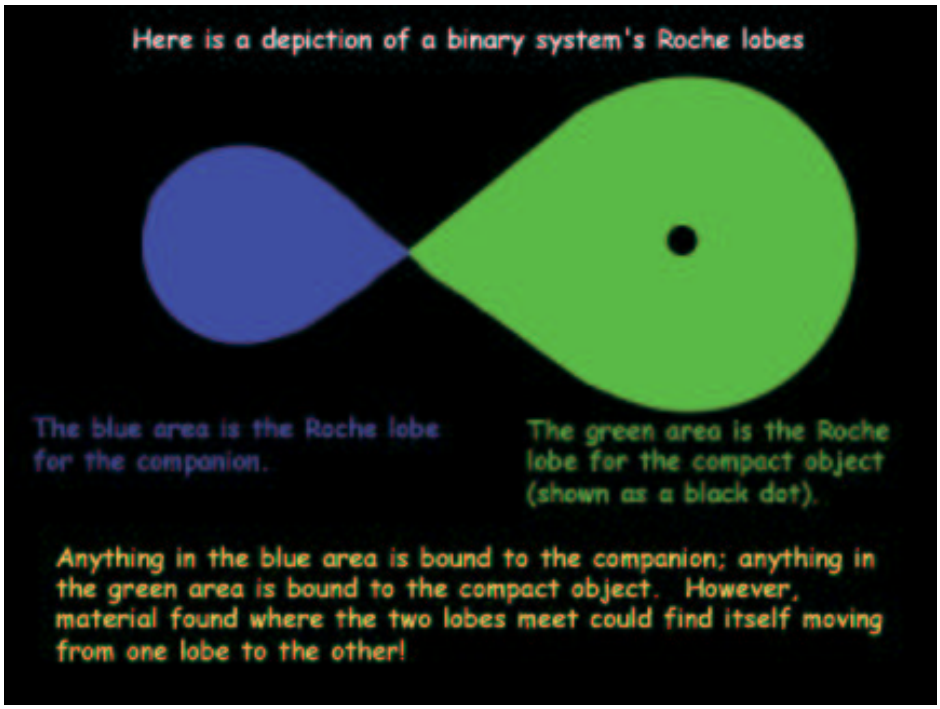

Figure 1: Roche lobe

This is a quantum mechanic effect that says that no more than one electron with the same quantum numbers can occupy the same energy state. The extreme densities inside white dwarfs force electrons to be in high energy states, where all the lower levels are filled.

In white dwarfs where the density is of the order 10^8 kg/m^3, the degenerate gas pressure is dominant, in spite of the high temperature. In the relativistic case P is proportional to $\rho^{4/3}$ and the transition to the relativistic case takes place at densities of about 10^9 kg/m^3. There is a limit for the mass a white dwarf can have because the degenerate electrons can not resist gravity any longer when the mass reaches the Chandrasekhar limit which is about 1.4 $M_\odot$. This limit is known as the Chandrasekhar mass M_{CH}.

1.4 Novae and Type Ia supernovae

Observations have shown novae to be members of close binary systems. One star of the system is a normal star while the other is a white dwarf.

The normal star fills its Roche lobe and material from it streams over to the white dwarf. When enough mass has been collected on the surface of the white dwarf, the hydrogen is explosively ignited and the outer shell is ejected. Within a day or two the brightness rises to a maximum, which may be 7–16 magnitudes brighter than the normal luminosity. This is followed by a gradual decline. As the ejected shell expands, the temperature of the star drops and the luminosity gradually decreases. The outburst does not stop the mass transfer from the companion star, so the white dwarf accretes new material for the next outburst. The emission and absorption lines from the expanding shell have expansion velocities of about 1000 km/s.

It is the accretion rate that determines whether the white dwarf will become either a nova or a supernova. If the rate of fusion is greater than the rate of accretion the result will be a nova, but if the accretion rate exceeds the fusion rate at the surface, more mass will be added to the white dwarf. When the mass comes close to M_{CH}, carbon fusion begins

at the centre and because of the degeneracy the rise in the temperature has no effect on the pressure. The star can not expand to slow the reaction rate, and a thermonuclear runaway results as the carbon fusion front rapidly moves toward the surface. This leads to a supernova Type Ia where the whole star is blown apart and there will be no remnant left.

2 Supernovae Type Ia

2.1 Explosion Models

2.1.1 Sub M_{CH} helium ignitors

In this scenario a carbon-oxygen white dwarf accumulates a helium layer. Detonations in the accreted helium layer have been suggested to drive a strong enough shock into the C-O core to initiate a carbon detonation. This might explain the class of subluminous explosion but these models disagree both photometrically and spectroscopically with observations (see Niemeyer et al. 2002).

2.1.2 Merging white dwarfs

This is a double degenerate scenario where two white dwarfs merge as a result of angular momentum losses via gravitational wave radiation (Renzini 1996). When the lighter WD have filled its Roche lobe, it is dissipated within a few orbital periods. It forms a disk around the more massive WD. This disk is accreted on the remaining WD via loss of angular momentum (Livio 2001).

If the accretion rate of C+O onto the remaining white dwarf is larger than a few times 10^{-6} $M_\odot$ yr^{-1}, the most likely outcome is off-center carbon ignition, leading to an inward propagating flame that converts the star into O+Ne+Mg. This configuration is unstable to electron capture onto ^{24}Mg and will undergo accretion-induced collapse to form a neutron star. Dimensional analysis of the expected turbulent viscosity suggest that it is very difficult to avoid such high accretion rates. This model can explain the absense of H and He in spectra (see Niemeyer et al. 2002).

2.1.3 The accreting Chandrasekhar mass WD

The favored model is a white dwarf that accretes matter from a binary red giant companion and explodes. Chandrasekhar mass WDs could be reached for relatively high accretion rates at about 10^{-8}– 10^{-7} $M_\odot$ yr^{-1}, the accreted hydrogen burns steadily on the surface allowing its mass to grow.

The strong temperature dependence of the nuclear reaction rates $\dot{S} \sim T^{12}$ at $T \simeq 10^{10}$ K (see Niemeyer et al. 2002), confines the nuclear burning to microscopically thin layers that propagate either conductively as subsonic deflagration (flames) or by shock compression as supersonic detonations. Both modes are hydrodynamically unstable to spatial perturbations. In the nonlinear regime, the burning fronts are either stabilized by forming a cellular structure or become fully turbulent, the total burning rate increases as a result of flame surface growth.

The first hydrodymamical simulation of a M_{CH} white dwarf (see Niemeyer 2002; Arnett 1969) assumed that thermonuclear combustion commences as a detonation wave, consuming the entire star at the speed of sound. Given no time to expand prior to being

burned the C+O material in this scenario is transformed almost completely into iron-peak nuclei and thus fails to produce intermediate–mass elements like O, Mg, Si, S, and Ca, in contradiction to observations. It is for this reason that the explosions are believed to begin in deflagration mode. A popular deflagration model is the W7 model (Nomoto et al. 1984) which can produce the observed element distribution quite accurate. The explosion starts as a deflagration near the centre of the star. Rayleigh-Taylor unstable blobs of hot burnt material are thought to rise and lead to shear-induced turbulence at their interface with the unburnt gas. This turbulence increases the effective area of the flamelets and, thereby the rate of fuel consumption (see Hillebrandt et al. 2000). Agreement with observations is best achieved if the burning front propagates at a substantial fraction of the sound speed. A slower speed does not make a supernova. Best agreement is achieved if a little over 1/2 of the mass of the white dwarf is turned into iron before expansion gradually quenches the burning.

Neither flames nor detonations can be resolved in explosion simulations on stellar scale and therefore have to be represented by numerical models. The length scales of physical processes range from 10^{-3} cm – 10^{7} cm (see Hillebrandt et al. 2000).

3 Type Ia Light curves

Although SNe Ia were originally believed to be all the same, they are now known to have a variety of light curve shapes, peak luminosities, and maximum–light spectra. The rise to maximum is very fast for a Type Ia supernova and it take about 18 days to reach maximum in the B–band. They can brighten by a half magnitude per day until about 10 days before maximum. Often the maximum in the B–band is taken to be the zero–point for the light curves. The peak phase starts about 5 days before the maximum is reached in the B–band, and at this time the peak in the infrared bands is reached. The peak phase can be approximated by Gaussian curves or second–order polynomials. The colors evolve rapidly around maximum, where they change from blue at about 10 days before maximum to red at about 30 days after maximum in the B–band. After maximum the supernova starts to fade slowly and go into a decline at blue wavelengths while in the redder wavelengths the decline decreases after about 20 days past maximum and shows a shoulder in R and a second maxima in IJHK bands. After about 50 days the light curves settle onto a steady decline which is exponential in luminosity, and the decline rates are the same for almost all SNe Ia, with a decline rate by about 0.014 mag/day in B, 0.028 mag/day in V, 0.042 mag/day in I, 0.043 mag/day in J, and 0.040 mag/day in H and K, between 50 and 120 days. At 150 days past maximum few objects has been observed. These have showed a change in the decline in the V, R and I filters between 120 and 140 days when the decline slows to 0.014 mag/day in V, 0.015 mag/day in R and 0.011 mag/day in I, while the decline rate in the B–band stays the same (Leibundgut 2000).

3.1 Bolometric light curves

We can not construct fully bolometric light curves, but only sum over the observed flux. Since this includes the near–UV, optical, and near–IR wavelengths, such light curves are often referred to as UVOIR. The contribution from the UV is expected to be less than 10% at maximum and the IR should not contribute significantly at that phase. The bolometric light curve has a secondary shoulder that shows up after about 20 to 40 days past maximum light. Compared to the massive SNe Type II, light curves of SNe Type Ia declines much faster because of the smaller mass of the progenitor and the high expansion velocities which makes the ejecta transparent to gamma–rays quicker.

The rise time of the light curve is determined by the explosion energy and how the ejecta becomes optically thin to thermalized radiation. The bolometric luminosity at maximum light is roughly equal to the instantaneous energy released by the radioactive decay from ^{56}Ni (Arnett's law), and can be used to determine the amount of nickel produced in the explosion. The late decline of the light curve is a combination of the energy input and at which rate this energy is converted to optical photons in the ejecta. The rise to and fall from maximum is slower for brighter objects and at late phases all SNe Ia shows the same decline rate.

It is the conversion of carbon and oxygen to iron peak and intermediate– mass elements that releases a large amount of energy initially, and later the $^{56}\mathrm{Ni} \longrightarrow {}^{56}\mathrm{Co} \longrightarrow {}^{56}\mathrm{Fe}$ decay powers the supernova through gamma–ray photons and positrons.

^{56}Ni decays by electron capture with a half–life of 6.1 days to ^{56}Co. The cobalt decays through electron capture (81%) and β^+ decay (19%) to stable ^{56}Fe with a half–life of 77 days. The γ–rays carry about 96.5% of the energy while the positrons carry 3.5% of the energy. During the earliest epoch after the SN explosion, the energy released in the $^{56}\mathrm{Ni} \longrightarrow {}^{56}\mathrm{Co} \longrightarrow {}^{56}\mathrm{Fe}$ decay is efficiently trapped by the SN ejecta. The deposition of this

energy creates energetic electrons, which thermalize and recombine. The optical photons created in the recombinations diffuse to the surface and escape the SN ejecta.

The shape of the light curve between 40 – 120 days past explosion is determined by the fraction of gamma–rays that are thermalized. The expansion of the SN ejecta lowers the column density to the surface and decreases both the time for optical photons to diffuse outward and the efficiency of trapping gamma–rays and energetic positrons and electrons. The SN thus makes the transition from an epoch where the energy deposition is essentially complete and instantaneous and the emission depends on the diffusion of optical photons, to an epoch where the diffusion timescale is negligibly short and the emission depends on the transport of the decay products.

At phases later than about 200 days the ejecta has became optically thin and virtually all gamma–rays escape freely from the ejecta. The luminosity is then provided by the kinetic energy deposited by the positrons in the ^{56}Co decay. The spectrum is dominated by collisionally excited Fe and Co lines. It has been assumed that the energy of the positrons in the ^{56}Co decay is locally deposited. This has been questioned because of the increased slope of the light curves (Milne et al. 2001), and it has been suggested that this is due to positron escape from the ejecta.

Whether or not the positrons are able to slip out of the ejecta depends on the strength and geometry of the magnetic field. If the magnetic field is weak and radially combed then there is a chance for the positrons to escape, but if the magnetic field is strong and tangled this would efficiently trap all the positrons, and keep the light curve at the radioactive rate. Previous attempts to study the positron phase of the light curve have been hampered by the lack of observational data. Cappellaro et al. (1997) had to use the assumption that the V–magnitude do follow the bolometric magnitude.

After about 450 days a thermal instability develops in the ejecta which rapidly cools down from about 3000 K to 300 K. Excitation of optical and infrared transitions decline rapidly and the cooling continues by fine–structure lines of Fe in the mid– and far–infrared regions. This is often referred to as the IR catastrophe (Fransson et al. 1996) but has not yet been observed in any SN Ia.

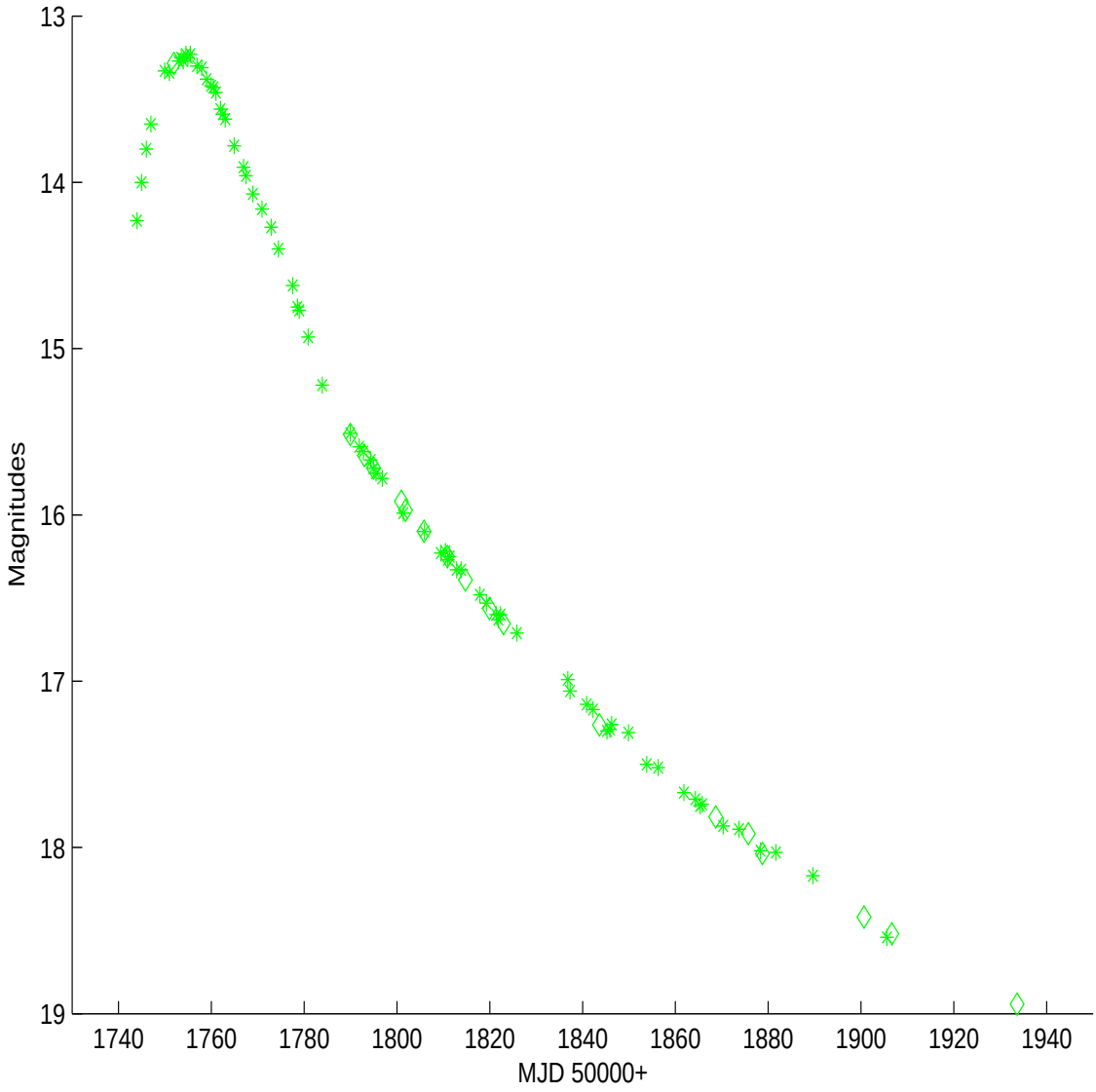

Figure 2: Light curve of SN Type Ia
This image shows how the V band light curve of SN 2000cx looks like. Data from Li et al. (2001).

4 SN 2000cx

SN 2000cx lies in the outskirts of the S0 galaxy NGC 524. It is positioned 23″ west and 109 ″.3 south of the nucleus. An image can be seen in figure 3. It was discovered by the LICK Observatory in unfiltered images taken on July 17.5 and 18.4 UT. A low–resolution optical spectrum on July 23 identified the event as a peculiar SN 1991T–like Type Ia with prominent Fe III absorption near 4300 and 4900 Å, but weak Si II at 6150 Å. This SN was the brightest SN that exploded in the year 2000. Its position far from the host galaxy in an uncrowded field and the fact that it was very bright, made it a good target to follow up for late time observations.

The early B–band light curve showed a peculiar evolution (Li et al. 2001). It brightened much faster than SN 1991T. The rise of SN 2000cx is just like that of SN 1994D which spectra show apparent differences from SN 2000cx. The pre–maximum brightening of SN 2000cx provides a counterexample to the correlation between spectroscopic peculiarity and light–curve behavior of SNe Ia. The light curve of SN 2000cx has a transition phase where the decline slows down six days after maximum light in the B–band. Because of this transition phase, SN 2000cx has a $\Delta m_{15}(B)$ value of 0.93±0.04 mag (Li et al. 2001). $\Delta m_{15}(B)$ is defined as the decline in magnitudes during the first 15 days after maximum brightness in passband B. As pointed out by Phillips (1993) and Hamuy et al. (1996), these $\Delta m_{15}(B)$ are good indicators of the luminosities of SN Ia in the sense that a SN Ia with a smaller $\Delta m_{15}(B)$ value, called a slow decliner, is more luminous than one with a greater $\Delta m_{15}(B)$ value (fast decliner). This light curve shape and luminosity correlation is often referred to as the luminosity–width relation.

The I band light curve for SN 2000cx showed a bigger dip between the two maxima than for other SNe, and the second maximum was fainter. The supernova was red in the B-V color during the rise time and up 10 days past maximum light, and it had a plateau phase between days 6–15 where the color curve had a nearly constant color of B-V= 0.3 mag, due to the plateau phase in the B band. After this the color turned blue and it remained so up to 90 days after maximum, when it settled on a constant value. The color up to 90 days was about 0.2 magnitudes bluer than the Lira–Phillips line (Phillips et al. 1999). The blue colors were also present in the V-R and V-I color curves.

SN 2000cx was a fast riser but a slow decliner and its light curve could not be fitted well by the different light curve fitting techniques that exists.

Among the SNe that has been compared to SN 2000cx by Li et al. (2001) SN 1991T is considered to be an over–luminous supernova, SN 1994D and SN 1992A are classified as normal supernovae, and SN 1991bg is an example of a subluminous supernova.

Early infrared photometry has been presented by Candia et al. (2003). The bolometric behavior of SN 2000cx, when compared to the normal SNe 1999ee and 2001el, showed that it rose to and fell from maximum more rapidly, and that the magnitude difference between peak brightness and 90 days past peak was larger than normal. This behavior is consistent with the higher kinetic energies seen at maximum light, but it can also be explained by this event being sub–luminous. SN 2000cx bolometric light curve differs from other Type Ia in the way that it has almost no secondary shoulder.

SN 2000cx was the brightest SN that year and was thus a very suitable supernova to do late time photometry. We have done observations in the optical and the near–infrared passbands at late times (360–480 days past maximum in the B band). Such near–infrared observations has never been done before and we can now see how important the near–infrared regions become when the ejecta has expanded and become cooler.

We want to construct a “bolometric” light curve from our observations and with this

we can do a comparison to the V band light curve and see whether the V band follows this bolometric light curve or not.

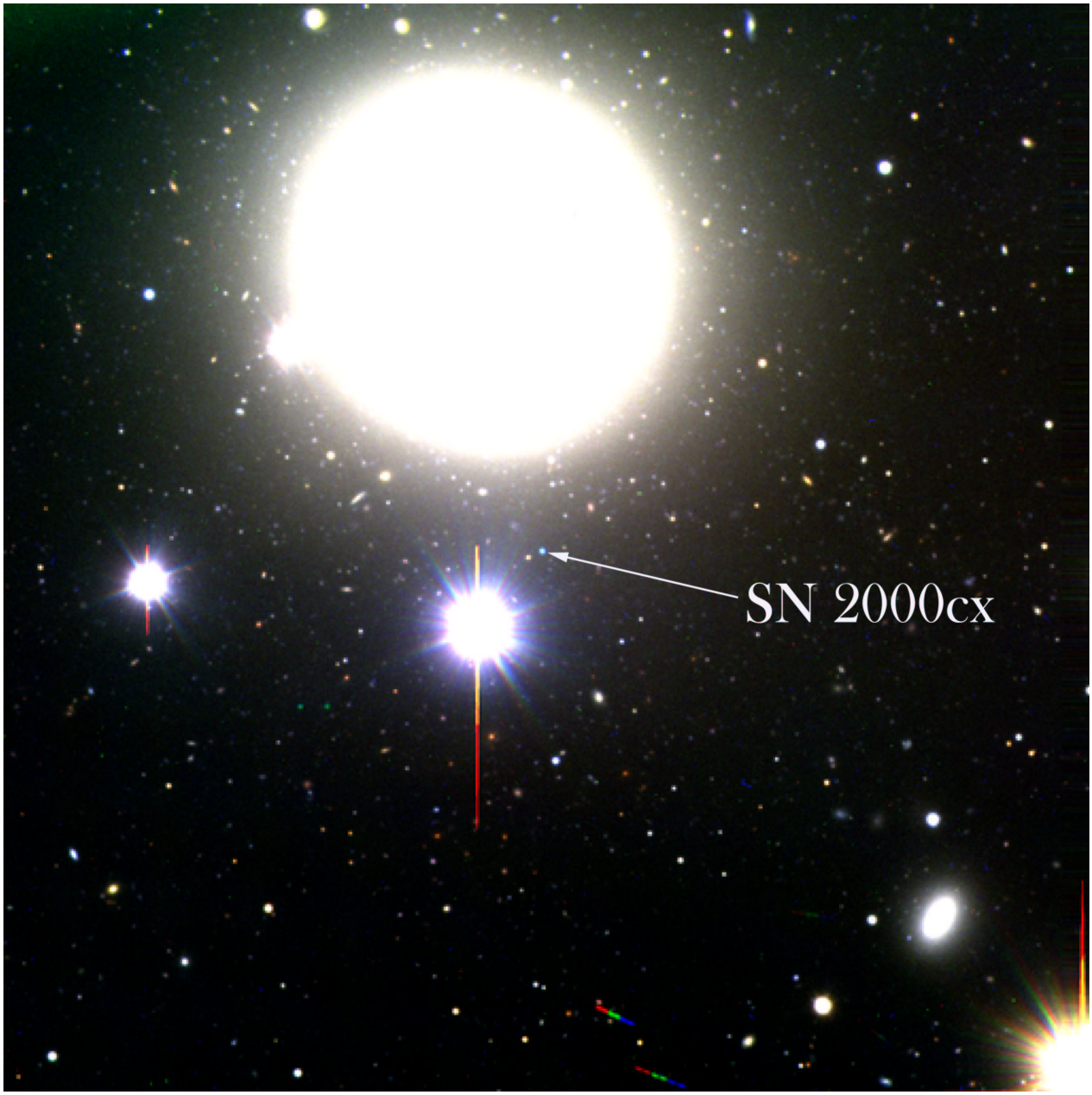

Figure 3: SN 2000cx
SN 2000cx and its host galaxy NGC 524. The field of view is $6.8' \times 6.8'$. This image is made with the IRAF task RGBSUN from three images. One B band image, one V band image, and one R band image. This is 360 days past maximum in the B band.

5 Optical Observations

5.1 Telescope

The observations were performed at the European Southern Observatory (ESO) Very Large Telescope (VLT), at the Paranal Observatory (Atacama, Chile), which consists of an array of four 8–meter telescopes which can work independently or in combined mode. In the combined mode the VLT provides the total light collecting power of a 16 meter single telescope. The useful wavelength range extends from the near UV up to 25 μm in the infrared.

The VLT optical layout (see figure 4) is of the Ritchey–Chretien type. The unit telescopes of the VLT can operate in either Cassegrain, Nasmyth or Coudé focus. The stellar light is collected by the primary mirror (M1), concentrated by the combination of the primary and the secondary mirror (M2) either directly to the Cassegrain focus located below the primary or to one of the two Nasmyth focii. The Coudé focus is obtained by transferring one Nasmyth focus to another location in the telescope basement by means of a relay system. From the Coudé focus the light can be sent to the combination mode focus or to the interferometric focus. When changing between Cassegrain and Nasmyth/Coudé operation, the curvature of M1 must be changed (active optics) and the secondary mirror must be refocused. At the Nasmyth foci as well as below the main mirror (the Cassegrain focus) astronomical instruments are mounted. These focii are accessible from the Nasmyth platforms and from the azimuth platform at the base of the telescope.

The Very Large Telescope uses active optics. The optical quality of the image is continually monitored by an image analyser using a reference star and the contributions of the various optical aberrations (defocus, astigmatism, coma, etc.) are computed. To achieve the best optical quality, discrete correction commands are given to the primary mirror support system, controlling the shape of the thin flexible M1, and to the M2 Unit, which controls the position of the M2 mirror along 5 degrees of freedom, namely one for focusing, two for centering, and two for pointing. The M2 mirror itself is configured as a rigid lightweight convex hyperboloid.

5.2 CCDs

CCD stands for Charge Coupled Device, and the detector consists of a surface that is made up of light–sensitive silicon diodes in a rectangular array. These diodes are called pixels. When a photon strikes the detector it can release an electron which will be trapped in a potential well inside the pixel. The quantum efficiency (QE), i.e. the number of electrons per incident photon, is high and the CCD is much more sensitive than a photographic plate. The CCD is nearly linear, which means that the number of electrons is directly proportional to the number of photons. Because one pixel only can store a certain number of electrons, it can be saturated if exposed to bright objects. After exposure, varying potential differences are used to move the accumulated charges row by row to a readout buffer. In the buffer the charges are moved pixel by pixel to an analogue–digital converter, which transmits the digital values to a computer.

5.2.1 Signal–to–noise

In a CCD image the measurement of the total flux from objects are made by counting the number of electrons released by the incident photons. This number of electrons is the signal (S). The measurement has some uncertainty which is called the noise (N). A large

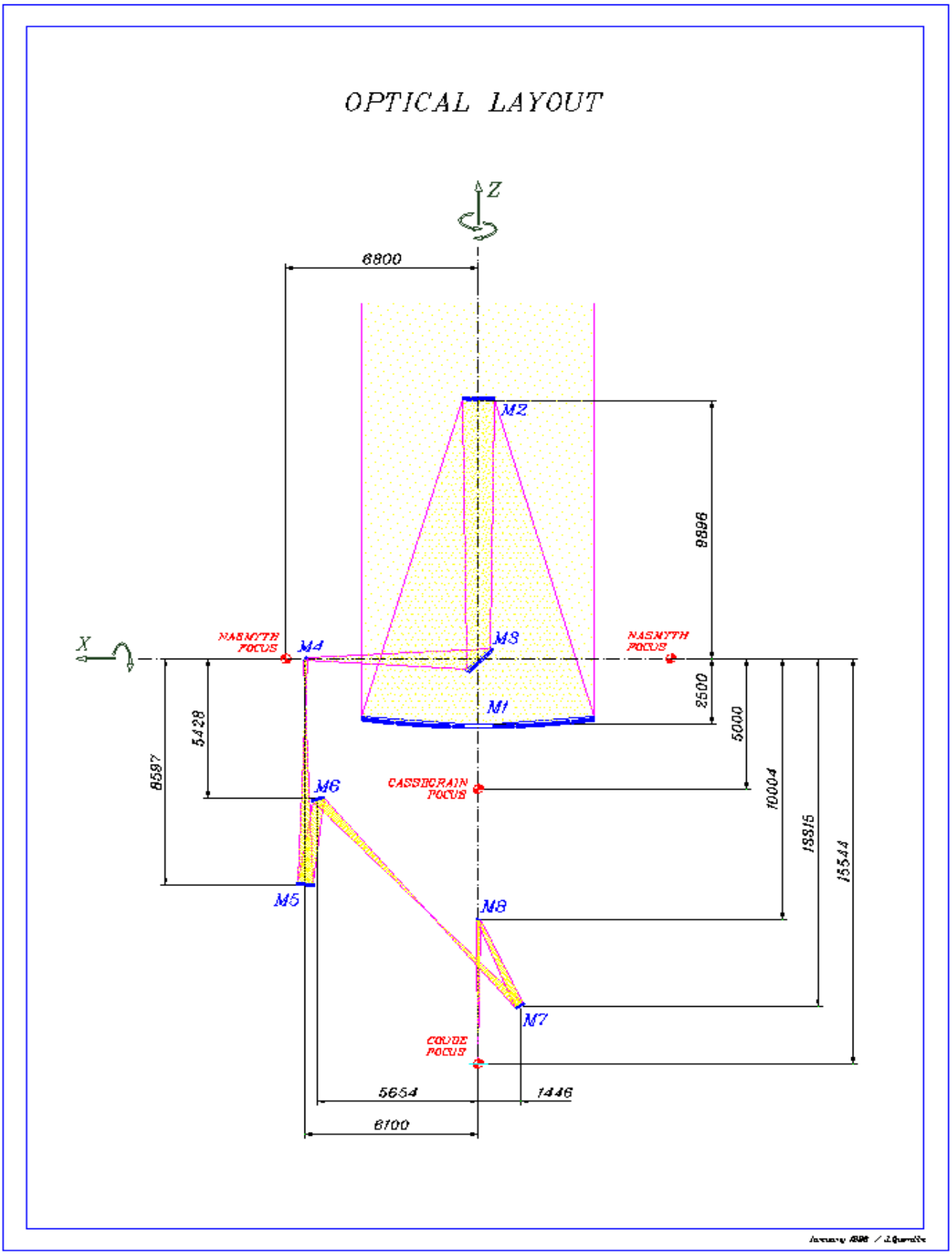

Figure 4: VLT optical layout

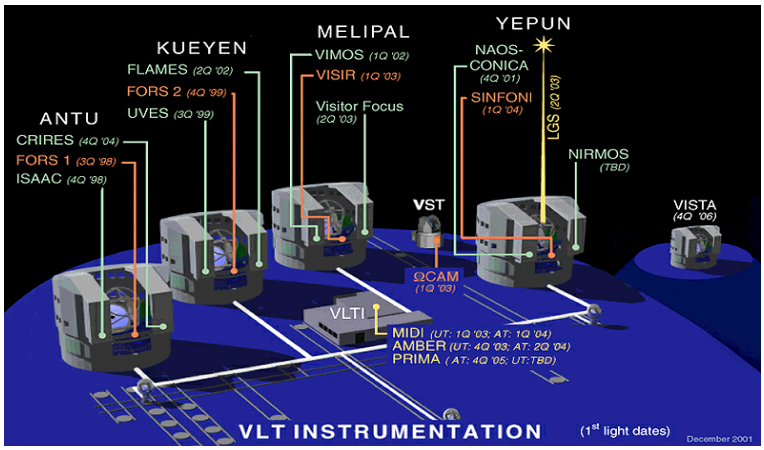

Figure 5: VLT instrumentation
The four unit telescopes of VLT with the different instruments and their location.

signal–to–noise ratio means that we can be very confident of the measured value of the signal. All electrons released by incident photons obey Poisson statistics.

The equation for the S/N of a measurement made with a CCD is given by

$$\frac{S}{N} = \frac{N_\star}{\sqrt{N_\star + n_{pix}(N_S + N_D + N_R^2)}} \tag{1}$$

The signal term in the above equation, $N_\star$, is the total number of photons (signal) collected from the object of interest. The noise terms in the above equation are the square roots of $N_\star$, plus n_{pix} (the number of pixels under consideration for the S/N calculation) times the contributions from N_S (the total number of photons per pixel from the background sky), N_D (the total number of dark current electrons per pixel), and N_R^2 (the total number of electrons per pixel resulting from the read noise). For sources of noise that obey Poisson statistics (which includes photon noise from the source itself), we know that for a signal level of N, the associated 1 sigma error (1σ) is given by $\sqrt{N}$. The above equation for the S/N of a given CCD measurement of a source can thus be seen to be simply the signal ($N_\star$) divided by the summation of a number of Poisson noise terms. The n_{pix} term is used to apply each noise term on a per pixel basis to all of the pixels involved in the S/N measurement and the N_R term is squared since the noise source behaves as a shot noise rather than being Poisson–like. We can also see from the above equation that if the total noise for the given measurement $\sqrt{N_\star + n_{pix}(N_S + N_D + N_R^2)}$ is dominated by the first noise term, $N_\star$ (i.e., the noise contribution from the source itself), then the CCD equation becomes

Filter name	eff. wavelength (nm)	FWHM (nm)
U BESS	366	36.0
B BESS	429	88.0
V BESS	554	111.5
R BESS	657	150.0
I BESS	768	138.0

Table 1: Fors1 Filters

Filter name	eff. wavelength (nm)	FWHM (nm)
U SPECIAL	362	29.0
B BESS	429	88.0
V BESS	554	111.5
R SPECIAL	655	165.0
I BESS	768	138.0

Table 2: Fors2 Filters

$$\frac{S}{N} = \frac{N_\star}{\sqrt{N_\star}} = \sqrt{N_\star} \tag{2}$$

5.3 Instruments

The two FORS (FOcal Reducer/low dispersion Spectrograph) instruments are designed as focal reducer multi mode instruments for the VLT. FORS is designed for the wavelength range from 330 nm to 1100 nm. Two spatial resolutions and hence field sizes can be selected by exchange of the collimators. The resulting field of view is $6.8' \times 6.8'$ with the standard resolution collimator (SR). The pixel size on the sky is $0.''20$. The detectors are 2048×2048 pixel Tektronix CCDs with 24 μ m pixels, thinned and anti-reflection coated. FORS contains a rotating half–segment shutter which guarantees uniform illumination of the CCD. We have used FORS 1 and FORS 2 for our observations. FORS 1 is attached to the third telescope called Melipal (see figure 5) and FORS 2 is attached to the fourth telescope called Yepun and both instruments are mounted at the Cassegrain focus.

5.4 Filters

SN 2000cx was observed in UBVRI passbands, where the U–band was only observed the first night of observations. The filters we have used for our observations are listed in table 1 and 2. These broad–band filters follow the Bessel (1990) system, which combine the Johnson and Cousins filter passbands.

6 Reductions

6.1 Bias–correction

To provide an estimate of the value produced by an unexposed pixel within a CCD, calibration measurements of the bias level can be used. To evaluate the bias or zero noise level and its associated uncertainty, specific calibration processes are used. The two most common ones are: overscan regions produced with every object frame or usage of bias frames. Overscan strips are a number of rows or columns or both that are added and

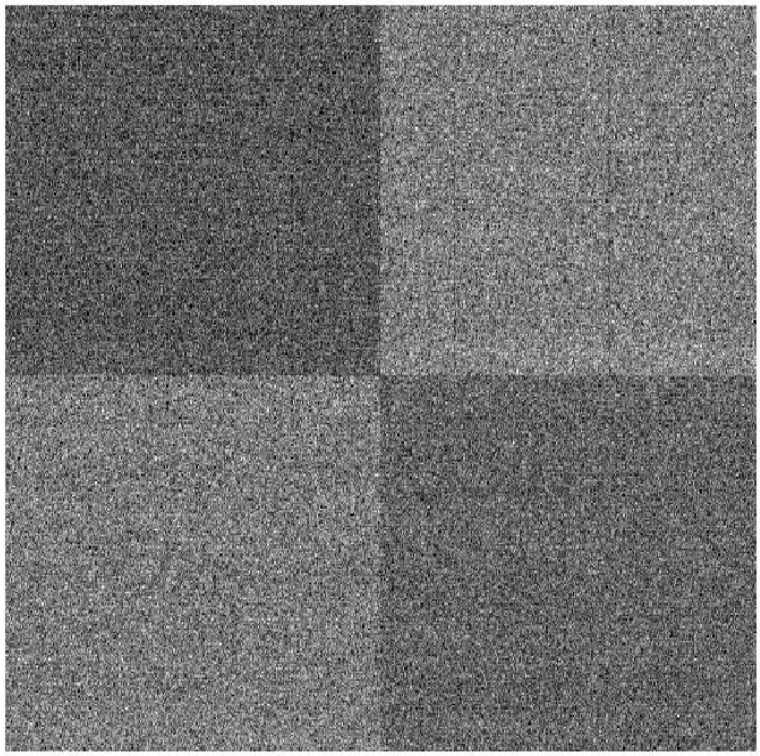

Figure 6: Bias image
A combined bias image where four quadrants can be seen. This regions are readout independently of each other in the 4 port readout mode.

stored with each image frame. Bias or zero images allow one to measure the zero noise level of a CCD. This type of CCD image has an exposure time of zero seconds. The shutter remains closed and the CCD is simply readout. A bias image is presented in figure 6.

6.2 Flat–field–correction

The idea of a flat field image is simple. Within the CCD, each pixel has a slightly different gain or QE value when compared with its neighbors. In order to flatten the relative response for each pixel to the incoming radiation, a flat field image is obtained (see figure 7) and used to perform this calibration. Ideally, a flat field image would consist of uniform illumination of every pixel by a light source of identical spectral energy distribution as that of the object. That is, you want the flat field image to be spectrally and spatially flat. Since the pixels within the array have different response to different colors of light, flat field images need to be obtained through each filter that is to be used for the science observations. As with bias frames, several flats exposed in each filter should be obtained and averaged together to form a master flat field, which can then be used for calibration of the CCD. Flat field exposures are used to correct for pixel–to–pixel variations in the CCD response as well as any nonuniform illumination of the detector itself. Flat fields are obtained by exposing the CCD to light from either a dome screen, the twilight sky, the nighttime sky, or a projector lamp in an attempt to provide a high S/N, uniform calibration image.

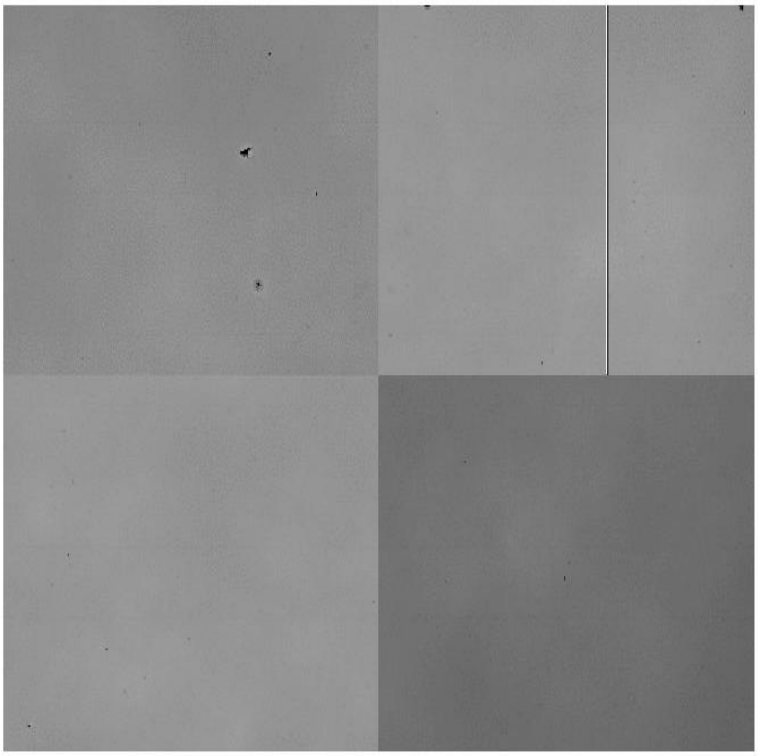

Figure 7: Flat field image
This is a twilight sky flat field image.

6.3 CCD Data Reduction

The process of standard CCD image reduction makes use of a basic set of images that form the core of the calibration and reduction process. This basic set of images consists of three calibration frames – bias, dark, and flat field – and the data frames of the object of interest. The use of the basic set of calibration images in the reduction of CCD object frames is as follows. First, subtract a mean bias frame from your object frame. Then, divide the resulting image by a (bias subtracted) mean flat field image. These two simple steps have corrected your object frame for bias level, and non uniformity within each image pixel (Howell 2000). In equational form, the calibration process can be written as

$$Final\,Reduced\,Object\,Frame = \frac{Raw\,Object\,Frame - Bias\,Frame}{Flat\,Field\,Frame - Bias\,Frame}$$

We have observations from four different epochs. These epochs are essentially July, September, October and November 2001 (see table 22 in the Appendix).

For the processing of our images we will use tasks in the package XCCDRED in IRAF, because we have a 4 port readout for all our images, so we can not use the same tasks as in the CCDRED package. All observations taken by the Very Large Telescope (VLT) can be found in lists provided by the European Southern Observatory (ESO). These observations are bias frames, flat field frames, standard star field images and field images where SN 2000cx is present. The first epoch of observations were taken with the FORS 2 instrument while all the other observations in the optical bands were taken by the FORS 1 instrument.

We began with making lists for the images that were taken during the same night, one list in each filter for the standard star- and the object images. We also made lists for the bias- and flat field images in the same way. Then we processed the bias images with the IRAF task ZEROCOMBINE in the XCCDRED package, and the flat field images with the task FLATCOMBINE. The flat field images were combined with zero–correction applied to them. Thus we have one combined bias image and one combined flat field image for each observation night. We can now apply the above equation to our raw object, and standard star field frames, to get the final reduced frames. A raw V–band image of the field can be seen in figure 8, and a reduced V–band image is presented in figure 9. The standard star- and the object images were processed with the task CCDPROC, the images were zero–corrected and flat–field–corrected, and we fitted the overscan vector interactively. Then we changed the name of all the standard star and object images so that they could easily be identified as a standard star or an object images. This was done with the command imrename.

```
imrename FORS2.2001-07-21T02:00:21.920.fits SA109-949_U_1.fits
```

This is the first U–band image for the standard stars in SA109–949. The other standard star images were named in the same way.

```
SN2000cx_1118_I1.fits
```

This is the first I–band image from the night 2001–11–18 and the other object frames have also their names from the night they were taken and in which filter plus a number.

Figure 8: Raw V-band image of SN 2000cx
This is how our raw images look like before any reductions is done.

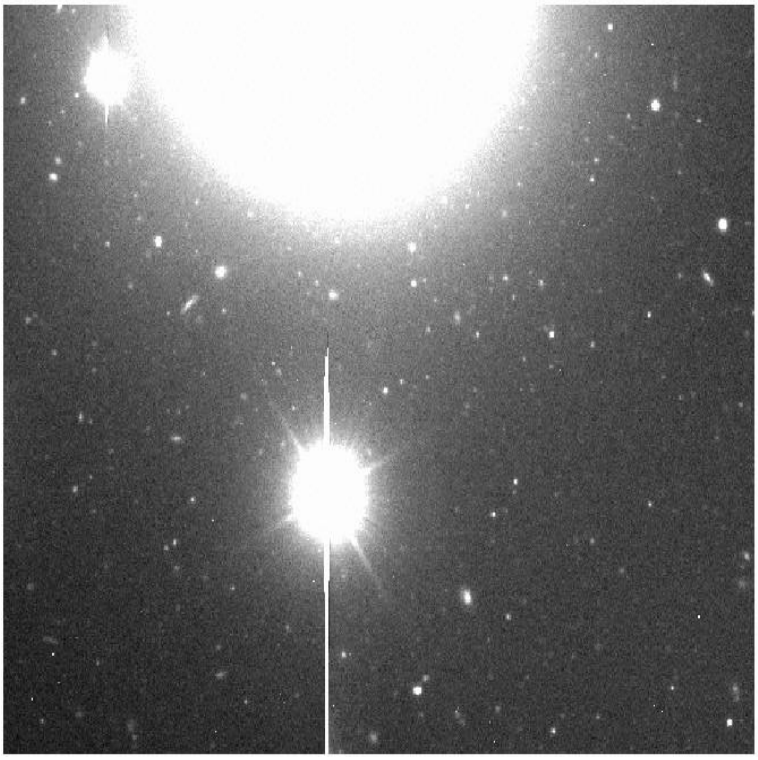

Figure 9: Reduced V-band image of SN 2000cx
This is the same image after bias subtraction and flat field division.

7 Photometry

7.1 Aperture Photometry

To obtain the absolute flux for an object, CCD frames of photometric standard stars are needed. These standard star frames are also used to correct for the Earth's atmosphere, color terms, and other possible sources of extinction that may be peculiar to a given observing site or a certain time of the year.

Aperture photometry is a technique that makes no assumption about the actual shape of the source PSF (Point Spread Function) but simply collects and sums up the observed counts within a specified aperture centred on the source. The basic application of aperture photometry starts with an estimate of the centre of the PSF and then inscribes a circular software aperture of radius r about that centre. The radius r may simply be taken as three times the full–width at half–maximum (FWHM). Summing the counts collected by the CCD for all the pixels within the area $A = \pi r^2$, and removing the estimated background contribution within A, one finally arrives at an estimated value for the collected source intensity I. The value of a magnitude is defined by the following standard equation:

$$m = z - 2.5 \log_{10} I + 2.5 \log_{10} exposure\,time \tag{3}$$

where z is the zero point and

$$I = S - n_{pix}\bar{B} \tag{4}$$

where $\bar{B}$ is the mean value of the background, and n_{pix} is the total number of pixels within that area.

7.2 Standard Stars

We have made standard star calibration for the first and the last epoch. The first epoch images were taken in July 2001, and the last epoch in November the same year. For the first epoch we have the following standard star fields: Mark A, PG1323 − 086, PG2331 + 055, and SA109 − 949. The images were reduced through zero–correction and flat field correction. We have one image in each of the UBVRI passbands for Mark A, PG1323−086, and PG2331+055, and we have three images in each band for SA109−949. The following standard stars in each standard star field were used (see table 3 and table 4).

Mark A	PG1323 − 086	PG2331 + 055	SA109 − 949
Mark A	PG1323 − 086	PG2331 + 055	SA109 − 949
Mark A1	PG1323 − 086A	PG2331 + 055A	SA109 − 954
Mark A2	PG1323 − 086B	PG2331 + 055B	SA109 − 956
Mark A3	PG1323 − 086C		
	PG1323 − 086D		

Table 3: First epoch standard stars

The standard star fields for the last epoch is: PG2213 − 006, Rubin 152, and SA100 − 269, where we have one image in each BVRI filters.

The standard stars were identified from templates containing the standard star field (Landolt 1992). The standard stars observed are Landolt standard stars, and this catalog is available within IRAF. Landolt has performed UBVRI photometric observations on

PG2213 – 006	Rubin 152	SA100 – 269
PG2213 – 006	Rubin 152	SA100 – 162
PG2213 – 006A	Rubin 152A	SA100 – 267
PG2213 – 006B	Rubin 152B	SA100 – 269
PG2213 – 006C	Rubin 152C	
	Rubin 152D	
	Rubin 152E	
	Rubin 152F	

Table 4: Last epoch standard stars

the Johnson–Kron–Cousins photometric system. All the Landolt standard stars that are present in our field will be used as a standard star. So we will have to identify the coordinates of these stars which we do with the task imexamine in interactive mode, point the cursor on a star and then press the a–key. The coordinates of the standard stars are now in coordinate lists, one for each standard star field.

For the photometry of our standard stars we have used the task PHOT in the DAOPHOT package. This task depends on other tasks in the DAOPHOT package so there are a number of parameters to be aware of. PHOT computes accurate centres for each object using the centreing parameters defined in the CENTERPARS task, computes an accurate sky value for each object using the sky fitting parameters defined in the FITSKYPARS task and computes magnitudes using the photometry parameters defined in the PHOTPARS task. The noise characteristics of the data are defined in the DATAPARS task.

To choose an aperture size we used the method described in, A User's Guide to Stellar CCD Photometry with IRAF by Philip Massey and Lindsey Davis (1992)[1], where we measured the flux with a big aperture size and a series of smaller ones, and then look for when the difference in flux between the big and the smaller aperture size gets constant. We then adopt this radius to be the radius for the photometry of all the standard stars in all the standard star fields. In our case this radius is 15 pixels, and we are using an inner aperture size of 30 pixels and an outer aperture size of 40 pixels to determine the sky background.

The CCD saturates at approximately 65000 counts, so we set the data max parameter to 61000 counts to avoid saturation. The stars which reaches over this limit will be flagged as INDEF.

7.3 Transformation Equations

When we have our observation file with the instrumental magnitudes, we would like to know the transformation equations so that we can compute the real magnitudes in each filter. The steps for finding the transformation equations are the following:

1. Create a catalog that contains the magnitudes and color indices of the standard stars on the standard system.

2. Create a standard star observations file that consists of the airmass, instrumental magnitudes and errors for each set of observations.

[1]http://iraf.noao.edu/iraf/web/docs/dockmain.html

3. Create a file containing the algebraic form of the transformation equations, and references to which columns in the tables contain which information.

4. Fit the transformation equations. This step is done interactively.

We run the task FITPARAMS to obtain these transformation equations, we do this fit interactively which will allow us to get rid of stars that makes a bad fit. FITPARAMS compares our instrumental magnitudes against the real magnitudes and compute the accurate transformation equations, the algorithm from Harris et al. (1981). In our case we are using Landolt (1992) as the standard star catalog and as the source for the transformation equations.

When we have transformation equations for one night we can use these equations on our object frames for the same night, to get the real magnitudes from our instrumental magnitudes in each filter.

We are solving the transformation equation

$$m = M + c_0 + c_1 C + c_2 X \tag{5}$$

where c_0 = zero point, c_1 = color term, and c_2 = extinction coefficient (see table 5). These three parameters were fitted with the task FITPARAMS. The color term and the extinction coefficients that we obtained from FITPARAMS were in fact very close to the values provided by ESO[2]. In this comparison we have adjusted our values so that they look like what we should have got if we were using the same transformation equations that ESO have used. ESO use the following equation:

$$M = m + c_0 + c_1 C - c_2 X \tag{6}$$

For the transformation equation parameters we finally decided to use the colorterm and extinction coefficient from ESO, because they have a larger set of observed standard stars. We also checked how the errors (from ESO) in these parameters affected the result. This was checked for the first epoch. The errors in these parameters are presented in table 6, and the difference between the magnitudes with no errors and when errors are considered is presented in table 7. The error in parenthesis are the standard deviation in magnitude for the local standard stars when errors in the transformation parameters are considered.

Table 5: Transformation parameters.

Date	Filter	Zero point	Extinction	Color term
2001 07 21	U	23.98	0.529, 0.442[a]	0.110, 0.092[a]
	B	26.82	0.219, 0.212[a]	-0.067, -0.067[a]
	V	27.16	0.115, 0.112[a]	0.014, 0.013[a]
	R	27.32	0.078, 0.074[a]	0.015, -0.031[a]
	I	26.38	0.033, 0.028[a]	-0.045, -0.046[a]
2001 11 20	B	27.20	0.383, 0.301[a]	-0.085, -0.084[a]
	V	27.52	0.107, 0.185[a]	0.036, 0.029[a]
	R	27.41	0.525, 0.130[a]	0.052, 0.018[a]
	I	26.57	0.347, 0.092[a]	-0.024, -0.037[a]

[a] Values by ESO.

[2]http://www.eso.org/observing/dfo/quality/FORS1/qc/qc1.html

Band	Extinction	Color
U	± 0.015	± 0.006
B	± 0.009	± 0.004
V	± 0.006	± 0.003
R	± 0.006	± 0.004
I	± 0.007	± 0.003

Table 6: Errors in the transformation parameters from ESO

	U	B	V	R	I
error +	0.0234 (0.0091)	0.0151 (0.0012)	0.0106 (0.0009)	0.0101 (0.0008)	0.0126 (0.0008)
error -	-0.0206 (0.0036)	-0.0154 (0.0012)	-0.0106 (0.0008)	-0.0100 (0.0009)	-0.0125 (0.0012)

Table 7: Changes in magnitude when errors in the transformation parameters are applied

The task INVERTFIT makes a catalog of the real magnitudes. The magnitudes are computed as differences between two colors except for the V magnitude, so the BV magnitude for the standard stars means that this is the $B - V$ magnitude. To get the B magnitude one has to compute $B = BV + V$. The Landolt standard star magnitudes and the errors from PHOT for the two epochs can be seen in tables 26 and 27 in the Appendix. The stars with INDEF as the magnitude are saturated and are not used in the computation of the transformation equations.

7.4 Local Standards

The reductions of our object images is done in the same way as for our standard star images. To align the images from each observation, and through the different epochs, we used imshift to do a rough estimation of the shifts in the images and then GEOMAP to get the proper shifts, and finally we used GEOTRAN to transform the images so that the stars will have the same coordinates in all the different images. This is because we want to use the same coordinate list for all images when we do photometry on the surrounding stars, and we also wish to combine the images in each filter from the same night. GEOMAP compares the coordinates from two different images, and computes the needed shifts to be done. These shifts are done by the task GEOTRAN. We always checked that the transformations have been done correctly by displaying them in a SAOIMAGE window, and then switch between the images to confirm that the stars appears in the same position. We combine the images taken during one night in the same filter with the task IMCOMBINE, where we do an average combining with no rejection, because when rejections were applied there were some strange effects on the images in some cases.

We selected 47 stars around the supernova from the object frames, and did photometry on these stars, because we want to use some of them as local standard stars. The instrumental magnitude were measured with an aperture of radius 6, an inner sky radius of 10 and an outer radius of 15. These magnitudes were then transformed to standard magnitudes by transformation equations and also aperture corrected to radius 15. We did aperture corrections with the task MKAPFILE.

We did this for both epochs and then compared the magnitude differences between all the object frames, to establish which stars that can be used as local standard stars. The magnitude difference must not be greater then 0.05 magnitudes if we want to use it as a local standard star.

From the 47 local standard star candidates (see tables 26 and 27 in the Appendix), we chose 14 which corresponds to our demands on magnitude differences. These are the stars that we will use as local standard stars when we do differential photometry to get the magnitudes for SN 2000cx for all epochs.

The instrumental magnitudes for our local standards computed by PHOT can be seen in tables 28–32 in the Appendix. The small letter indicates the filter and the four digits are month and date. The magnitudes for the 14 standard stars are listed in table 8, where the position to the standard stars from SN 2000cx are marked as an offset in arc seconds and the direction from the supernova (figure 10). The magnitudes are the mean magnitude for the two epochs and the errors are the square root of the errors from PHOT in quadrature plus the mean error of the difference between the epochs in quadrature. For the U–band the errors are the errors from PHOT plus the errors from the transformation equations since we have only U–band observations for the first epoch.

7.5 Aperture Corrections

Because we have measured the Landolt standard stars with an aperture of radius 15, and our local standards with an aperture of only radius 6, we need to do an aperture correction from 6 to 15. This is done using the task in IRAF called MKAPFILE. We measured the magnitudes of the local standard stars with the aperture of 6, 7, 8, 9, 10, 11, 12, 13, 14, and 15 pixels, and then run MKAPFILE. The result is a file where the corrections in magnitude and the errors are computed.

Aperture corrections were performed with three different sets of stars. These sets consisted of just one relatively isolated star in the field, our 14 standard stars and the 47 stars that were selected from the beginning. How the magnitudes should be corrected and the corresponding errors depend on how we choose to do the aperture corrections, as presented in tables 33–38 in the Appendix. The final aperture corrections were made using the 14 standard stars and interactively excluding stars that obviously did not fit the curve in the IRAF task MKAP. The final values are listed in table 9.

7.6 Photometry of SN 2000cx

We can do photometry on the supernova using the task PHOT in DAOPHOT. The photometry is done with the same parameters as for our local standard stars. We performed

Offset arcsec	U	B	V	R	I
115.12 E, 17.86 S	23.69 (0.17)	23.29 (0.04)	22.45 (0.02)	21.99 (0.02)	21.48 (0.02)
134.48 W, 154.34 N	21.59 (0.05)	21.54 (0.03)	20.77 (0.02)	20.28 (0.01)	19.75 (0.01)
140.48 W, 88.12 N	24.16 (0.18)	23.04 (0.03)	21.48 (0.02)	20.55 (0.01)	19.54 (0.01)
52.08 E, 116.12 N	22.59 (0.07)	21.95 (0.02)	20.86 (0.02)	20.22 (0.01)	19.57 (0.01)
40.55 E, 106.03 N	22.73 (0.07)	22.62 (0.04)	21.80 (0.01)	21.29 (0.02)	20.72 (0.02)
158.45 W, 45.25 S	22.40 (0.07)	23.17 (0.04)	22.37 (0.01)	21.83 (0.02)	21.28 (0.03)
156.22 W, 187.75 S	21.52 (0.05)	21.68 (0.01)	21.18 (0.02)	20.85 (0.02)	20.47 (0.01)
188.73 W, 6.06 N	24.13 (0.20)	23.04 (0.02)	21.60 (0.02)	20.70 (0.02)	19.66 (0.01)
24.84 E, 12.28 S	24.51 (0.26)	23.59 (0.04)	22.69 (0.03)	22.14 (0.03)	21.49 (0.03)
62.29 E, 9.51 S	24.55 (0.25)	23.89 (0.05)	22.97 (0.03)	22.44 (0.03)	21.82 (0.04)
68.48 E, 121.36 N	23.01 (0.10)	23.10 (0.02)	22.14 (0.02)	21.59 (0.01)	20.94 (0.01)
109.51 E, 180.10 S	23.77 (0.14)	23.57 (0.04)	22.85 (0.03)	22.38 (0.03)	21.86 (0.03)
88.22 E, 78.11 N	23.02 (0.09)	23.09 (0.02)	22.34 (0.02)	21.87 (0.02)	21.32 (0.02)
82.48 W, 104.51 N	23.86 (0.15)	24.05 (0.05)	22.92 (0.03)	21.99 (0.03)	21.17 (0.03)

Table 8: Magnitudes of local standards

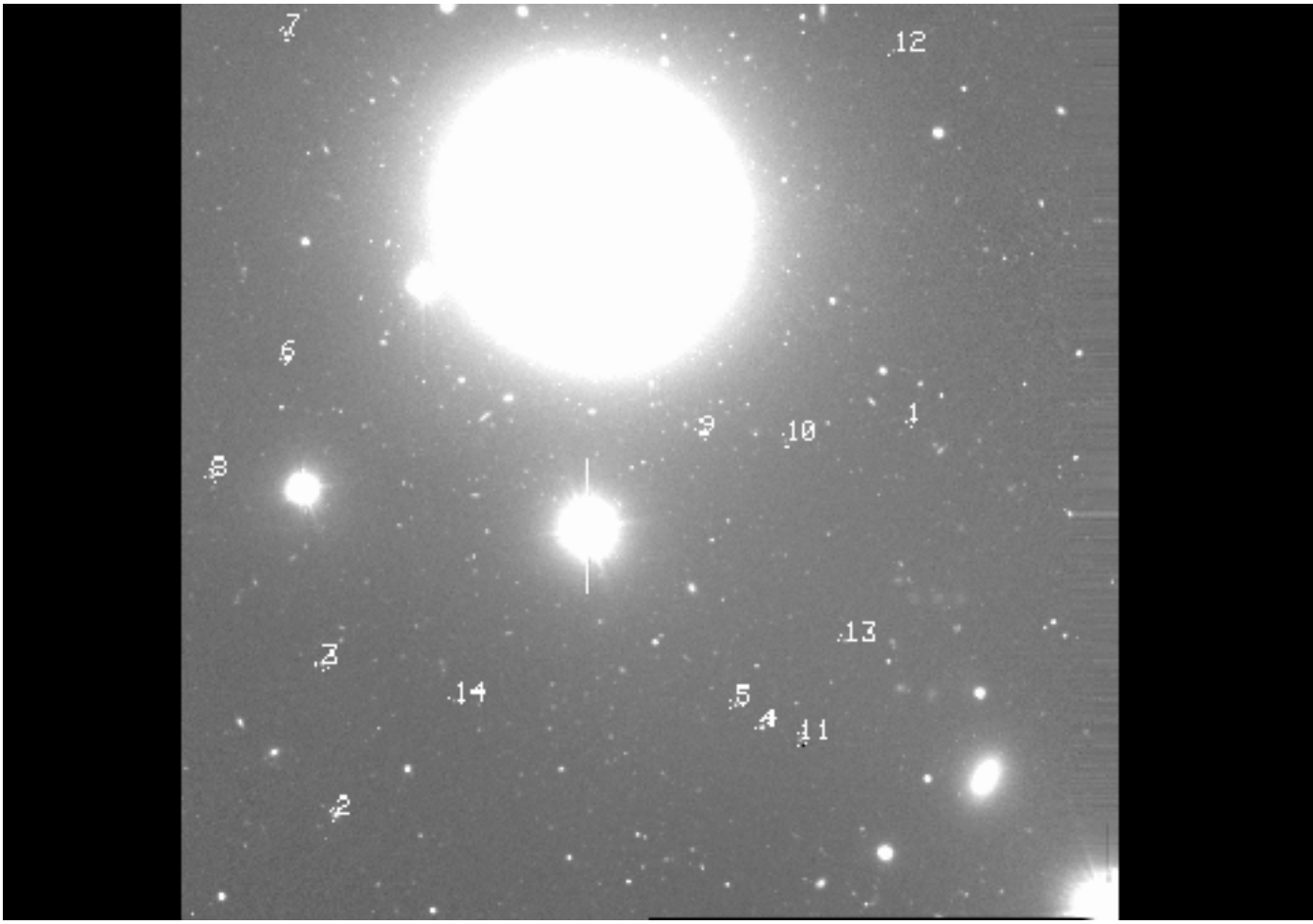

Figure 10: Local standard stars
The 14 standard stars that we have used to determine the magnitudes for SN 2000cx.

Date	Filter	Magnitude	Error in magnitude
0720	U	-0.296	0.016
0720	B	-0.292	0.014
0720	V	-0.214	0.011
0720	R	-0.171	0.008
0720	I	-0.148	0.007
1119	B	-0.199	0.010
1119	V	-0.177	0.008
1119	R	-0.196	0.009
1119	I	-0.151	0.007

Table 9: Aperture corrections

differential photometry for SN 2000cx to get the real magnitudes for each night. We computed the difference between the instrumental magnitudes for SN 2000cx and our local standard stars. The instrumental magnitudes for SN 2000cx in the different bands for each night are presented in table 11. Because we have established the real magnitudes for our local standard stars we can now add this magnitude to the difference, and in this way we will get the real magnitude for the supernova (see table 10). The magnitude of SN 2000cx will be the mean value of the 14 magnitudes we get from the differential photometry and the errors are the standard deviation plus the errors from PHOT. These errors are summed in quadrature and then the square root of these terms will be taken as the error for the supernova magnitude. The dates are presented in Modified Julian Days (MJD).

Table 10: Late optical magnitudes for SN 2000cx.

MJD[a] 52000+	Phase[b] (days)	U	B	V	R	I
111.4	359	22.30 (0.08)	21.27 (0.03)	21.28 (0.01)	22.17 (0.02)	21.70 (0.03)
112.3	360			21.28 (0.03)		
165.3	413		22.00 (0.03)	22.02 (0.03)	22.91 (0.03)	22.09 (0.03)
192.1	440				23.26 (0.04)	
199.2	447		22.50 (0.03)	22.46 (0.01)		22.42 (0.03)
201.2	449				23.46 (0.03)	
232.5	480		23.00 (0.04)	23.03 (0.02)	23.85 (0.06)	22.84 (0.05)

[a] Refers to the first image of the ObsID.
[b] Days past maximum B-band light

Date	u	b	v	r	i
0720	24.12 (0.05)	20.08 (0.01)	19.47 (0.01)	20.12 (0.02)	20.57 (0.03)
0721			19.57 (0.01)		
0912		20.44 (0.01)	19.90 (0.01)	20.80 (0.02)	20.80 (0.02)
1009				21.39 (0.03)	
1016		20.88 (0.01)	20.22 (0.01)		21.11 (0.02)
1018				21.37 (0.03)	
1118				21.78 (0.06)	21.59 (0.04)
1119		21.46 (0.01)	20.90 (0.02)		

Table 11: Instrumental magnitudes of SN 2000cx

Filter	Decline rate Mag/100 days
B	1.42
V	1.44
R	1.37
I	0.94

Table 12: Late decline rates for SN 2000cx

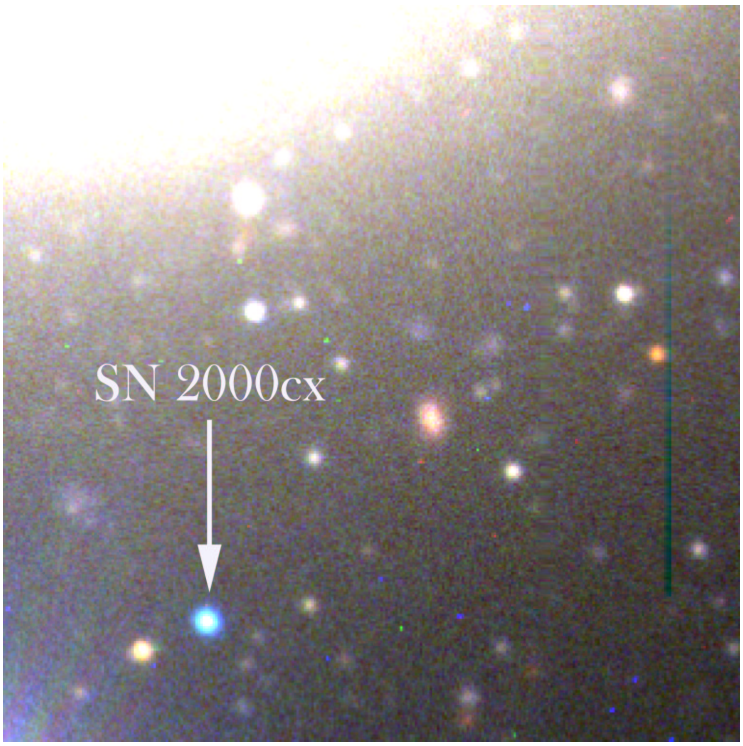

Figure 11: SN 2000cx, July 2001
The supernova 360 days past maximum in the B band. This image was obtained with the IRAF task RGBSUN, and it is a colored image made from B, V, and R band images.

Figures 11 and 12 show SN 2000cx at the first and the last epoch respectively. We can see that the supernova has faded and the magnitudes for the different epochs and filters are plotted figure 13. The decline rate in the B–band is 1.42 magnitudes per 100 days, 1.44 mag/100 days in the V–band, 1.37 mag/100 days in the R–band, and 0.94 mag/100 days in the I–band (table 12). The color evolution of the different passbands are shown in figure 14. We can see that SN 2000cx gets redder in the V-I color curve, while the other color bands show no color evolution. The B-V color curve are essentially zero for all epochs, and the V-R color curve lies around -0.9 mag.

Comparison of SN 2000cx with other SNe Ia are shown in figure 15. Both SN 1992A and SN 1996X are classified as normal SNe Type Ia. The data are shifted so that maximum in the B band occurs at the same date and at the same magnitude. The dates here are days past maximum in the B band. The overall feature for these SNe at late times is that they decline in the same fashion and that SN 2000cx behaves like a normal supernova at late phases.

Figure 12: SN 2000cx, November 2001
The supernova 480 days past maximum in the B band. It is clearly seen that the supernova has faded compared to figure 11.

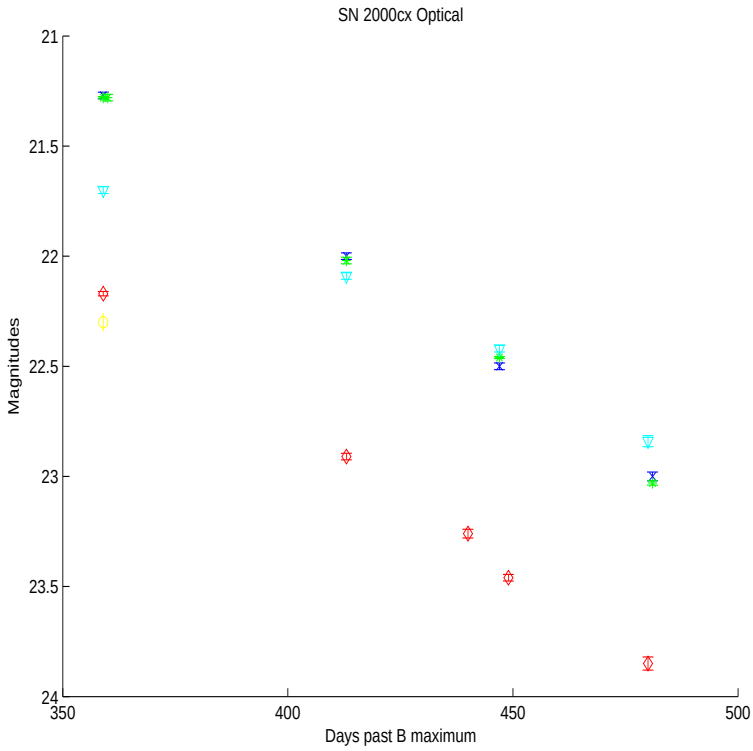

Figure 13: Optical magnitudes of SN 2000cx
V=Green *, B=Blue x, R=Red ⋄, U=Yellow o, I=Cyan △
The errors are ± the errors from table 10

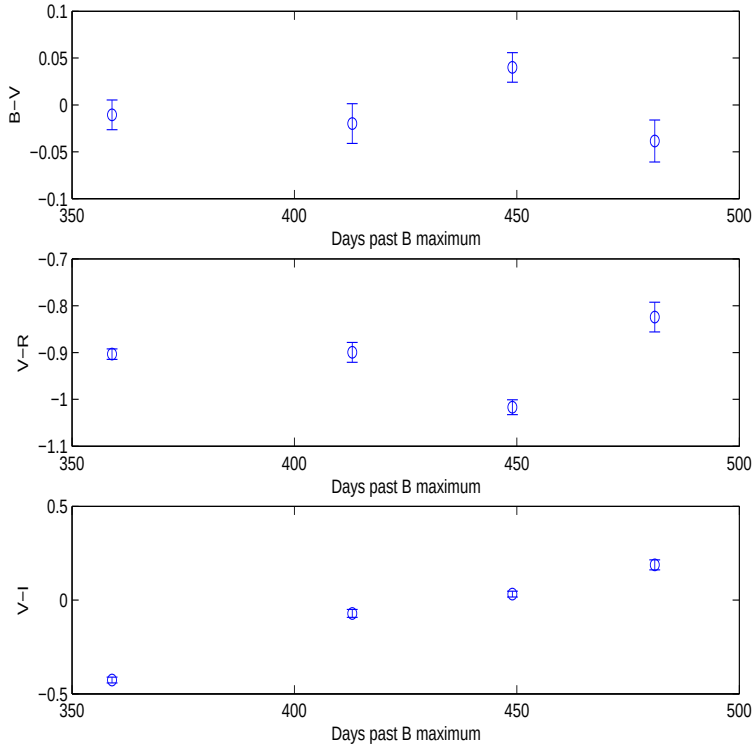

Figure 14: Color evolution of SN 2000cx
The V-I color curve evolves to the red.

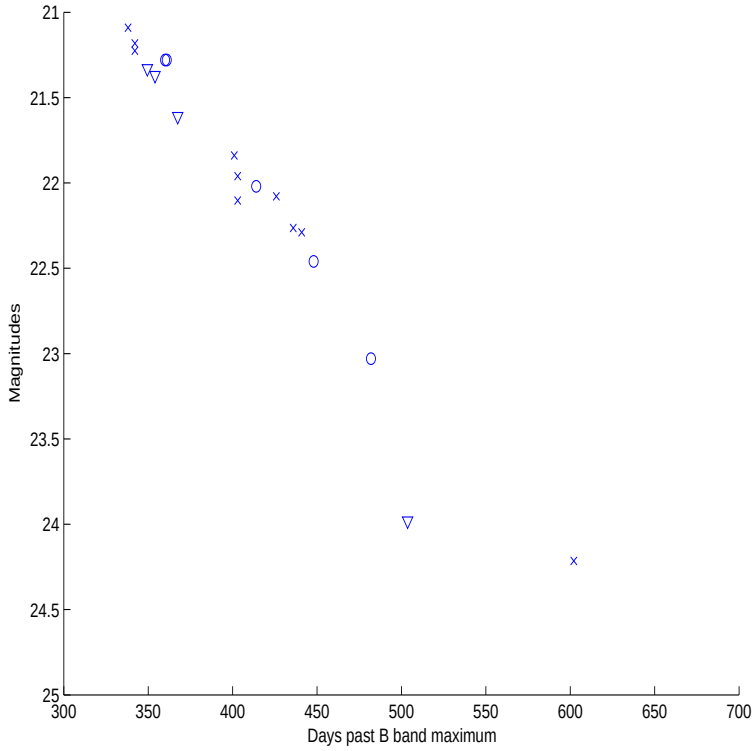

Figure 15: SN 2000cx, SN 1992A, and SN 1996X at late times.
We show here the V band for SN 2000cx compared to two normal supernova. They are shifted to have the same magnitude in the B band at maximum, which is also shifted to occur at the same time for the three SNe.
SN2000cx (o), SN 1992A (x), and SN 1996X (triangles)

8 Infrared Observations

We have also performed near infrared observations using the Infrared Spectrometer And Array Camera (ISAAC). ISAAC is attached to the Nasmyth B focus of the first telescope, Antu, of the four VLT telescopes. In the short wavelength (SW) imaging mode, the Rockwell Hawaii HgCdTe 1024×1024 array detector was used. The pixel size on the sky is $0.''147$ and the field of view is $2.'5 \times 2.'5$. There is no shutter, so the array is continuously exposed to light. We observed the supernova in the J, H and K_s bands. The wavelengths for these filters are shown in table 13.

Filter	Wavelength (μm)	Width (μm)
J	1.25	0.29
H	1.65	0.30
K_s	2.16	0.27

Table 13: IR filters

We have calibration– and object images taken on 2001–07–30, 2001–09–20, 2001–11–18, 2001–11–19 and 2001–11–21 (table 39 in the Appendix). The dark exposures are combined with the ECLIPSE task *isaacp dark*. We have the following exposure times for the calibration- and object images.

- 3.5 seconds of exposure time for the standard star images.
- 5.0 seconds of exposure time for the flat field images.
- 12.0 seconds of exposure time for the Ks filter images.
- 15.0 seconds of exposure time for the H filter images.
- 30.0 seconds of exposure time for the J filter images.

Three dark images are available for each exposure time. The flat field images are combined in the task *isaacp twflat*, and these images is dark subtracted in the combining task with the 5 seconds of exposure dark image. Dark frames are exposures without detector illumination. The detector bias is a function of the Detector Integration Time (DIT), so the DIT of the science data and that of the dark must match. The dark frames are combined and subtracted from the science frame, just like the bias frame for the optical data.

We have used the task *jitter* to do the sky background subtraction for both the standard star– and the object frames. Jitter imaging is an effective method to take care of the sky background with a minimum loss of observing time. By observing the same spot on the sky with small offsets around a central object, it is possible to determine the sky background variations by filtering the images and separate astronomical objects from sky signal. The first frame in each observation is centred on the object of interest and the following frames are offset from the first position. When observing point–like sources most of the observed signal will be the sky background. Sky combination is a method used to filter out low frequency sky variations from a set of jittered images. One estimated sky frame is obtained per input raw frame. The method is iterating on each pixel position on the detector along a time line. This gives an array of $\pm$h pixel values around each

pixel, which will then be scaled by the average value of the plane it was extracted from. The scaled array is sorted by increasing pixel value, and the reject min and reject max pixel values will be rejected. The h value is the half width of the running time filter. The default value in the jitter.ini file is set to 7, which means that in the best case 15 frames (minimum 8) are used for each pixel to estimate the sky variations. The reject min and reject max parameters are the number of rejected lower and upper pixels. Their sum shall not exceed the half width value. Rejecting low–valued pixels compensates for very noisy values, while rejecting high–valued pixels is the mechanism which extracts the astronomical objects. The default value for both these parameters are 3.

The method works poorly when a pixel position sees mostly an object signal and not a sky background variation. Then it becomes difficult to discriminate sky from object signal. This is the case for extended and bright objects. When jittered around, the offsets are never big enough to prevent skewed estimates. The resulting artefacts are usually dark crowns surrounding the bright objects in the final image, which can affect the photometry. The offsets for the standard stars were determined by header keywords while for the object frames we had to give this in a file. The offsets were determined by displaying the images and then check how the stars changed position from one frame to another. For the epochs where we have more than 15 images in a filter, there will be two images with the same offset so we divide these epochs into two image sets so that no star will have the same offset twice. We also created an object file where we gave the coordinates of stars that are present in all frames for the producing of one final image from the input frames.Then we combined these two images in the same fashion as we did for the optical images. This time we used the IRAF tasks XYXYMATCH, IMALIGN, and IMCOMBINE. For JITTER ,we used the parameters:

reject half width=7, reject min=3, reject max=3

8.1 Transformation Equations

The transformation equations have the form:

$$J = mJ + j1 + j2 \cdot XJ \tag{7}$$

mj is the instrumental magnitude in filter J, j1 is a constant (zero point), j2 extinction and XJ is the airmass in filter J. The same equations are used for the H and K_s bands. The match between the ISAAC filters (J, H and K_s) and those used to establish the faint IR standard star system of Persson et al. (1998) are quite good, so we expect the color terms to be small and we will drop this term in our transformation equations. We used the averaged extinction parameter from ESO [3](table 14).

We solved the transformation equations for the epochs 2001–07–30 and an average of the three nights of observations for the last epoch. We have only one standard star for the first epoch and in total five standard stars for our last epoch.

8.2 IR Standard Stars

The standard star magnitudes are from Persson et al. (1998) and Casali & Hawarden (1998). The photometry was performed in the same way as for the optical photometry. The standard star catalog will look like the Landolt standard star catalog with the name of the standard stars and their magnitudes (table 15).

[3]Average values from ESO.
http://www.eso.org/instruments/isaac/imaging_standards.html

Date	Filter	Zero point	Extinction
2001–07–30	J	24.823 (0.02)	0.11
2001–07–30	H	24.592 (0.02)	0.06
2001–07–30	K_s	24.043 (0.03)	0.07
2001–11–18 — 2001–11–21	J	24.952 (0.002)	0.11
2001–11–18 — 2001–11–21	H	24.602 (0.003)	0.06

Table 14: Transformation Equations in Infrared

Date	Standard star	Filter	Magnitude	Exposure
2001–07–30	S279–F	J	12.477	10x3.5
		H	12.118	10x3.5
		K_s	12.031	10x3.5
2001–11–18	S234–E	J	12.464	5x3.5
		H	12.127	5x3.5
2001–11–19	S234–E	J	12.464	5x3.5
		H	12.127	5x3.5
2001–11–21	FS10	J	14.749	5x3.5
		H	14.870	5x3.5
	FS19	J	13.565	5x3.5
		H	13.654	5x3.5
	FS32	J	13.459	5x3.5
		H	13.576	5x3.5

Table 15: Infrared Standard Stars

The local standard star candidates were chosen all over the images, and they were in total 35 isolated and quite bright objects. We then applied the late transformation equation to our instrumental magnitudes on the late epoch. The magnitudes that we get for each night in the late epoch is summed and then divided by three to get an average magnitude for the late epoch. The errors from PHOT will also be an averaged value. To get a catalog of the real magnitudes we use the task EVALFIT which produces a catalog with the magnitudes in our different filters. Then a comparison is made between the real magnitudes, for the first and the last epoch, and if the difference is not greater than 0.1 magnitudes in both the J and H filters we will use that star as a local standard star. This resulted in 14 standard stars for our infrared observations (see table 16). The local standard stars that we have used are in figure 16.

The real magnitude of each standard star is computed by summing the magnitudes in the two epochs and then divide this by two. The errors are the square root of the errors from PHOT in quadrature plus the mean of the difference between the epochs in quadrature for filter J and H, while for the K_s filter the errors are the ones produced by PHOT.

J	H	K_s
18.10 (0.06)	17.47 (0.03)	17.15 (0.01)
20.23 (0.08)	19.22 (0.06)	18.35 (0.03)
18.45 (0.06)	17.84 (0.02)	17.57 (0.02)
19.87 (0.05)	19.07 (0.04)	18.77 (0.04)
18.30 (0.05)	17.66 (0.03)	17.29 (0.02)
16.08 (0.04)	15.42 (0.01)	15.14 (0.01)
17.54 (0.05)	17.12 (0.02)	17.02 (0.01)
19.03 (0.06)	18.31 (0.03)	18.10 (0.02)
20.37 (0.07)	19.72 (0.07)	19.55 (0.06)
18.29 (0.06)	18.14 (0.03)	17.87 (0.02)
21.13 (0.07)	20.47 (0.07)	20.07 (0.09)
20.94 (0.06)	20.46 (0.07)	20.23 (0.10)
20.37 (0.07)	19.70 (0.05)	19.50 (0.06)
20.01 (0.07)	19.04 (0.04)	18.14 (0.02)

Table 16: Infrared Local Standards

8.3 SN 2000cx in IR

The infrared magnitudes of SN 2000cx were computed by differential photometry, in the same way as we did for the optical bands. The magnitudes for the last epoch seems to vary by about 0.2 in magnitude (see table 19 and figure 17). The instrumental magnitudes that was used in the calculation are presented in table 18, and the instrumental magnitudes for our local standard stars can be found in tables 40–44 in the Appendix.

The images produced by jitter had some dark areas around very bright or extended objects, so we tried to do the the reduction steps also using the IRAF task XDIMSUM to check if there could be any differences in the photometry.

In this way we were able to get rid of the dark areas but there were no significant difference in the obtained photometry. We then tested the photometry on objects with about the same magnitude as SN 2000cx for the last epoch, and we found that the standard deviation in the magnitudes for these faint objects were around 0.3 in magnitude both with jitter and XDIMSUM. The error estimates provided by PHOT are thus probably too optimistic and we believe that the errors are better represented as 0.3 mag for the faint supernova.

This was done by choosing 10 stars with about the same instrumental magnitudes as the supernova. One of the stars were then set to an arbitrary real magnitude, and differential photometry was done for the three nights in the last epoch. Then we computed the standard deviation for the nine stars which showed the result above.

The aperture corrections (table 17) were made by choosing a couple of bright isolated stars from the images taken during the same night as for which the transformation equations were established. The infrared images of SN 2000cx for the first and the last epochs shows that the supernova appears to have the same magnitude, figures 18 and 19, which agree with our measurements.

With the error estimate of 0.3 mag we can say that the supernova stays at a constant magnitude during all epochs in the J band and also in the H band. Because this is the first time that near–infrared photometry has been carried out for a Type Ia supernova at these late phases, we can not compare SN 2000cx to other SNe. Color evolution is present

in both V-J and V-H, because we have shown that the V band steadily decreases while the near–infrared bands are at a constant magnitude. The color clearly evolves to the red (see figure 20).

Date	Filter	Magnitude	Error in magnitude
0730	J	-0.071	0.005
	H	-0.037	0.003
	K_s	-0.034	0.002
1118	J	-0.159	0.009
	H	-0.085	0.006
1119	J	-0.121	0.007
	H	-0.063	0.004
1121	J	-0.348	0.017
	H	-0.157	0.010

Table 17: Infrared Aperture Corrections

Date	j	h	k_s
0730	21.92 (0.08)	21.70 (0.13)	21.25 (0.11)
0920	21.94 (0.07)	21.48 (0.09)	
1118	21.97 (0.09)	21.58 (0.13)	
1119	21.80 (0.09)	21.34 (0.11)	
1121	21.54 (0.10)	21.54 (0.10)	

Table 18: Infrared instrumental magnitudes SN 2000cx

Date	MJD	J	H	K_s
2001–07–30	52120	21.86 (0.08)	21.33 (0.13)	20.32 (0.11)
2001–09–20	52172	21.83 (0.07)	21.05 (0.10)	
2001–11–18	52231	21.87 (0.09)	21.15 (0.14)	
2001–11–19	52232	21.73 (0.09)	20.95 (0.12)	
2001–11–21	52234	21.77 (0.11)	20.99 (0.11)	

Table 19: Infrared magnitudes SN 2000cx

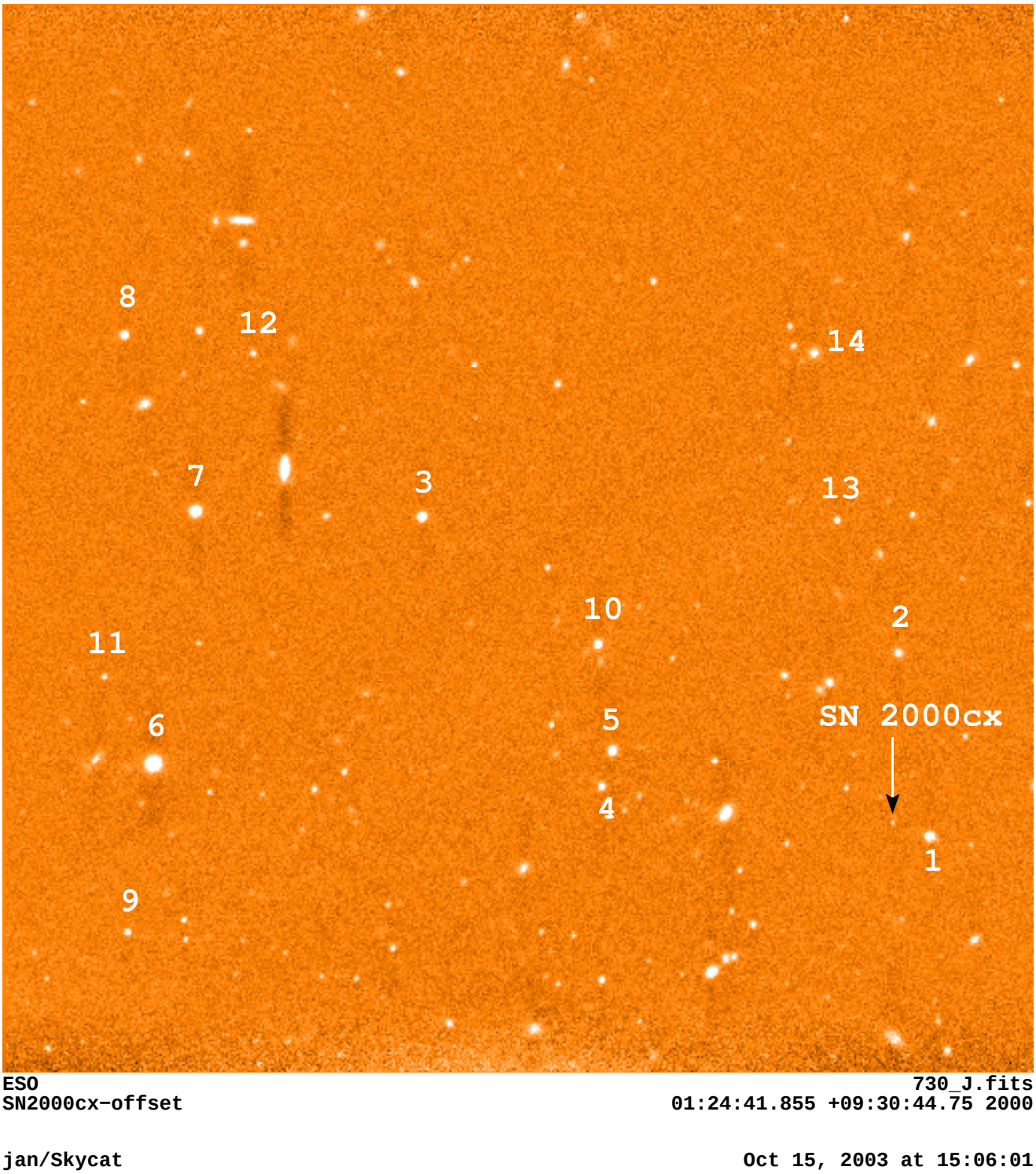

Figure 16: Local standard stars in IR
The 14 standard stars together with SN 2000cx. The field of view is $2.'5 \times 2.'5$.

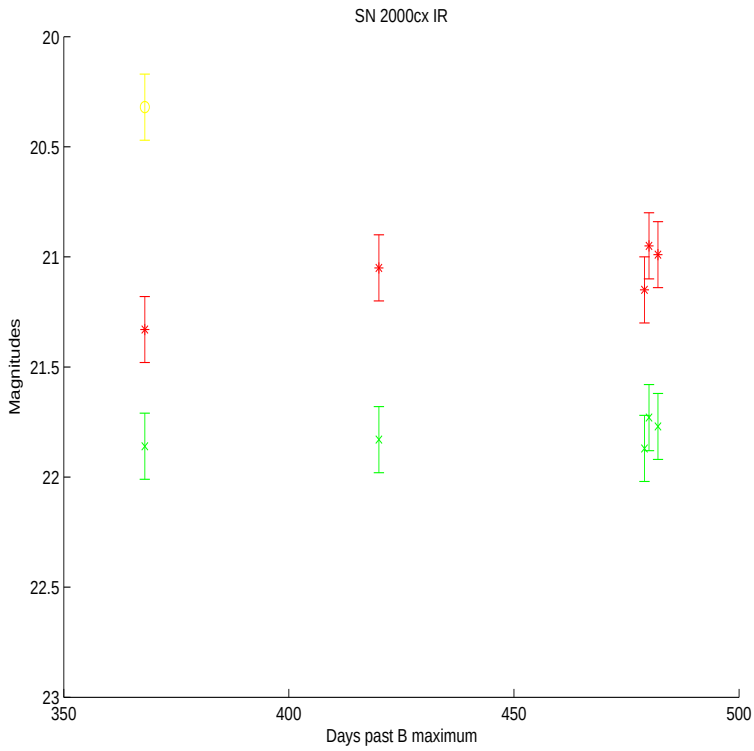

Figure 17: IR magnitudes of SN 2000cx
J=Green x, H=Red *,K_s=Yellow o. The errorbars are the estimated error from the photometry and are $\pm$ 0.15 mag.

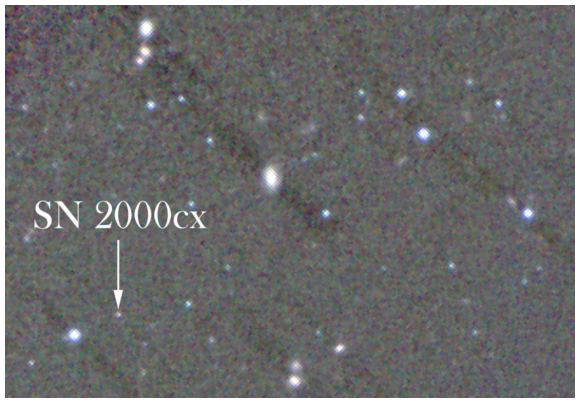

Figure 18: SN 2000cx, July 2001
Near–infrared image of the supernova 370 days past maximum. This image was obtained with the IRAF task RGBSUN, which produces an colored image from one J band, one H band, and one K_s band image.

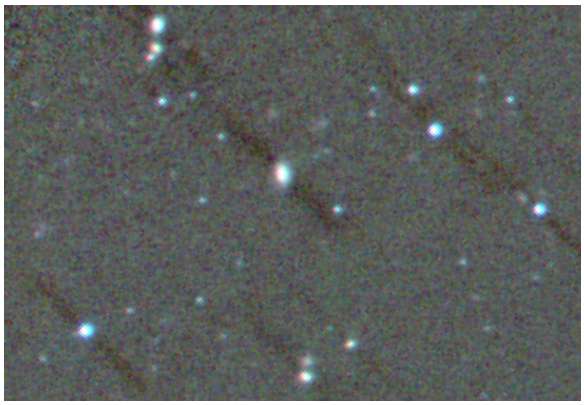

Figure 19: SN 2000cx, November 2001
Same as the previous image but the supernova is now at 480 days past maximum. There is no apparent magnitude difference compared to the previous image, although this image is taken 110 days later.

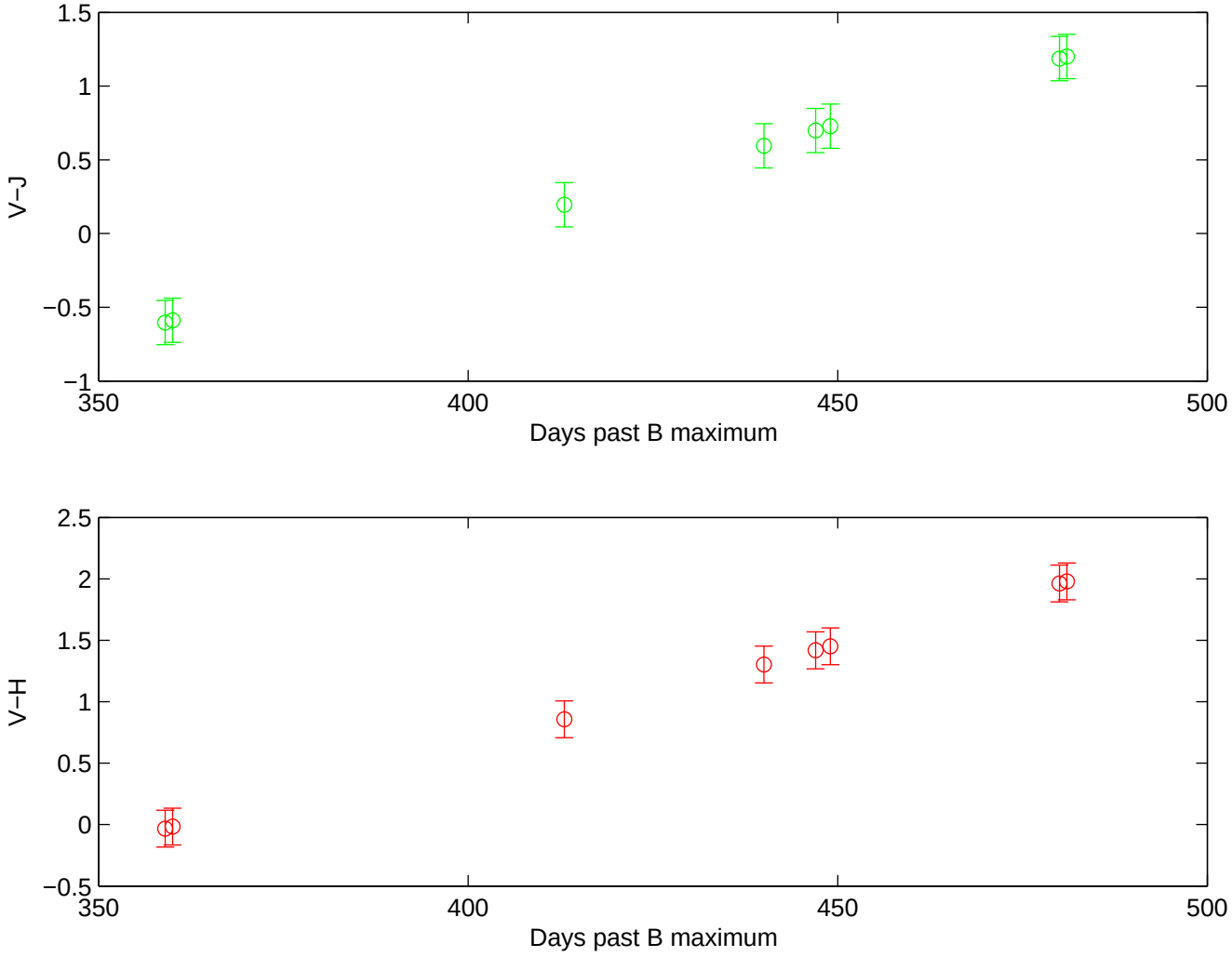

Figure 20: Color evolution of V-IR
The V band and the IR bands are linearly fitted to their magnitudes. The fitted values are plotted here, the errorbars are ± 0.15 mag.

9 Discussion

Observations of late SNe Type Ia light curves are not common. Only a few exists up to date in the optical bands. The late observations that exists are mainly done in the V band and in the B band. Light curves in the near–infrared passbands that has been done up to date do generally not cover later times, but only times up to around 100 days past maximum. Assumptions have been made that there is no bolometric correction for the V band and that this band follows the bolometric light curve at late times. This is based on the bolometric light curves that has been done at early phases from the observed optical and near–infrared light curves (Suntzeff 1996). Model–generated bolometric light curves have been made where the V band represents the bolometric light curve. Observed SNe light curves at later times seem to fall faster than expected from models. A possible explanation have been that positrons created in the cobalt decay manage to escape the ejecta. This would lead to less energy deposited in the ejecta and to a faster decline of the bolometric light curve.

We have observed the late time light curve behaviour of the Type Ia supernova SN 2000cx in both optical (UBVRI) and near–infrared (JHK) bands. The observations were done between 360 and 480 days past maximum light for four epochs in the optical and three epochs in the near–infrared. Such infrared observations have not been done before at these late phases.

Elias et al. (1983) have done near–infrared observations of three SNe Type Ia at late times, SN 1981B, SN 1980N, and SN 1981D between 140 to 373 days past maximum. SN 1981B were observed a couple of days around 140 days, SN 1981D has only one point at around day 280, and SN 1980N were observed at 230 days and at 373 days. None of the SNe are well covered at late phases. They show that the decline rate after 100 days is similar at all wavelengths and that the V-IR colors are not particularly red (V-H color is about -0.4 at 100 days). The red J-H color at 100 days is about 1.6 and it gets bluer at some time after 120 days, but their data are not very accurate.

With our new observations, we can test the assumption that the V band light curve can be used as a bolometric light curve, by constructing a bolometric light curve at late phases and compare this to the V band light curve at these times.

9.1 The bolometric light curve

The fast expansion of the ejecta would result in a very rapid decline in luminosity if only the thermal energy from the explosion had been available to power the supernova. However, the observed supernova light curves show that the decline is rather slow, and 150–200 days past maximum light the light curve declines almost linearly which corresponds to an exponential luminosity decline.

The late light curve is powered completely by the radioactive decay of ^{56}Ni which is produced in explosive silicon burning. ^{56}Ni is unstable and decays into ^{56}Co emitting γ–rays, but the half–life of ^{56}Ni is relatively short (6.1 days) so this decay can only be important at early epochs. ^{56}Co is also unstable and further decays to ^{56}Fe releasing γ–rays and positrons. Because of its longer half–life the ^{56}Co (77 days) decay can power the light curve for several years. Positrons are produced in the radioactive β^+ decays of ^{56}Co. About 96.5 % of the energy released in the decay are carried by the γ–rays and 3.5 % of the energy by positrons.

In early phases of SN evolution the density of the ejecta is still high enough to trap γ–rays in the ejecta and completely thermalize this through Compton scattering with the

free electrons. In the expansion, the density decreases and the mean free path of the γ–rays increases and the ejecta becomes transparent to optical radiation a few months after maximum light.

At around 200 days past maximum the trapping of the γ–rays has decreased and the kinetic energy of positrons starts to dominate the energy input to the ejecta.

The positrons are the dominating energy input at the time of our observations. The late light curves of SN 2000cx, 360 to 480 days past maximum light, shows a decline in all optical bands while the light curves stay constant in the near–IR bands. The decline rates are 1.42, 1.44, 1.37, and 0.94 mag/100 days in the B, V, R, and I bands respectively.

That the infrared magnitudes stay constant indicates that the importance of the IR contribution increases with time, when more of the emission is emitted at these wavelengths.

To construct the bolometric light curve of SN 2000cx we need to know the distance and extinction towards the supernova. Extinction is caused by the absorption and scattering of light by interstellar dust grains.

An effect caused by the interstellar medium is the reddening of light, blue light is scattered and absorbed more than red light. Studies of the interstellar medium show that the ratio of the visual extinction A_V to the color excess $E(B-V)$ is almost constant for all stars $R = A_V/E(B-V) \approx 3$. The apparent magnitude in filter V is given by

$$V = M_V + 5\log_{10}(r/10pc) + A_V, \tag{8}$$

where M_V is the absolute magnitude in filter V and r is the distance in parsec. The bolometric light curve has been constructed by integrating over the observed flux. To get the flux we convert our magnitudes to flux from the equation

$$m = -2.5\log_{10} f + constant, \tag{9}$$

where m is the measured magnitude and f is the flux in that passband.

We assume that the U band follows the B band and that the near–infrared magnitudes do not change between the time when the optical and near–infrared observations were done in the same epoch. For the missing epoch in the near–infrared, the third epoch in optical, we assume that the magnitudes are the same as they are in the last epoch, and that K_s has a constant magnitude during all epochs. Reddening from the host galaxy NGC 524 is not expected since this is an early–type galaxy and SN 2000cx is positioned where no contamination is expected. Early spectra shows that SN 2000cx do not show any signs of the narrow interstellar Na I D absorption at 5940 Å. There is an absorption feature at 5890 Å which is caused by interstellar Na I which indicates Galactic reddening towards the supernova. The Galactic reddening for SN 2000cx is $E(B-V) = 0.08$ mag (Li et al. 2001).

We use the parameters $E(B-V) = 0.082$ and $R = 3.1$ for the calculation of the extinction in the different passbands. The extinction curve is from Fitzpatrick (1999). We then integrate over all wavelengths for each of the epochs we have. The distance modulus is $m - M = 32.47$ from Candia et al (2003).

$$m = -2.5\log_{10}\int F d\lambda \tag{10}$$

We then convert the integrated flux to magnitudes for the bolometric light curve and we compare this to the converted V band flux.

$$M_{Bolometric} = -2.5\log_{10} F - 32.47 \tag{11}$$

where F is the integrated flux.

The two light curves are matched to have the same magnitude at 380 days past maximum (see figure 21). The two light curves do not follow each other. Instead the V band light curve deviates more from the bolometric light curve with time. The slope of our bolometric light curve is 1.22 mag/100 days, which is steeper than the Co decay with an instantaneous deposition of the decay energy which is expected to be 0.98 mag/100 days.

9.2 Positron escape

The assumption that the V band reflects the bolometric luminosity has been made in previous investigation of positron escape. Milne et al. (1999, 2001) states that light curves can be reproduced only if a substantional fraction of the positrons escapes the ejecta, and here they assumed that the V–band follows the bolometric luminosity (no color evolution). In 1999 they studied 10 SNe where five of them could be fitted if positron escape was assumed while for the remaining five they found no evidence for positron trapping. The observations were done in the V and B bands. They considered 21 different models and made model–generated bolometric light curves which was compared to the observed ones. They assume little color evolution at late times and that the V band is the best single band to trace the bolometric light curve.

In 2001 they studied 22 SNe in BVRI. These were divided into three subclasses: normally luminous, sub–luminous, and super–luminous. The categorization is based upon the $\Delta m_{15}(B)$ values. The normally luminous–sub–luminous cut were at $\Delta m_{15}(B)$ =1.60 and the normally luminous–super–luminous cut at $\Delta m_{15}(B)$ =0.95 mag. They normalized all SNe to have zero magnitude at 65 days after explosion when the photon diffusion timescales becomes negligible. The 16 normally luminous and super–luminous SNe in their sample did not need to be differentiated into distinct subclasses after day 60. If the V band scales with the bolometric emission the late emission from all 16 SNe could be explained with a single light curve if positron escape were assumed. After day 150, the V band data could explain all sub luminous models if positron escape is assumed.

They also found for the R band and the I band for the three subclasses were similar at late times, and they determined the color evolution from measured spectra. Some color evolution occurs during day 60 to day 200 with no further color evolution beyond day 200.

Positrons are also connected to the magnetic field in the supernova in the sense that positron escape depends on the strength of the magnetic field. If positrons do escape this would give a steeper light curve, whereas a strong magnetic field would trap the positrons and the light curve would then approach the radioactive decay rate.

Positron transport depends on the magnetic field. Three scenarios have been suggested to model the magnetic field (Ruiz–Lapuente & Spruit, 1998). The first suggests that the field is too weak to confine positrons and that positrons follow straight–line trajectories, with a fraction escaping the ejecta (Colgate, Petschek & Kriese 1980). The second suggests a stronger field that confines positrons, but the field lines are radially combed by the homologous expansion. The positrons can spiral along these radial field lines with a fraction escaping the ejecta (Chan & Lingenfelter 1993). The third scenario suggests a strong field that is turbulently disordered. Positrons may survive non–thermally at late times, but none escape. Colgate et al. (1980) argued that the first two situations are equivalent. Differing positron escape leads to differences in model energy deposition rates, which makes late observations of SNe Ia a probe of the photon and positron transport.

Ruiz–Lapuente & Spruit (1998) show that if convection has developed in the WD core

during the pre supernova evolution, a tangled magnetic field should have grown in the WD. This is expected to occur in C+O Chandrasekhar WDs but not in sub–Chandrasekhar WDs. If the pre–explosion magnetic field of the WD is less than $10^5 - 10^8$ G positrons could be able to escape.

If positrons manage to escape the ejecta, the time at which the departure from the full trapping scenario takes place can provide estimates of the original magnetic field of the WD, its configuration, and also of the mass of the supernova ejecta.

Several factors can induce changes in the evolution in luminosity within a sample of SNe of the same type: different distributions of radioactive material, different masses of the ejecta, and different magnetic field configuration.

Magnetic fields of WDs have been measured, and they range from 10^5 to $5\times$ 10^8 G. If the magnetic field lines do not contribute to confine the path of the energetic positrons, with energies in the MeV range, a fraction of this energy escapes the ejecta and the evolution in luminosity of the SN is affected, there will be a steeper decline of the light curve.

Capellaro et al. (1997) studied 5 SN that were selected to represent the known range of absolute luminosities at maximum. They found that observations requires a range of a factor of 10 in the masses of the radioactive material synthesized in the explosion ($M_{Ni} = 0.1 - 1.1 M_{\odot}$), and a factor of two in the total mass of the ejecta ($M_{ej} = 0.7 - 1.4 M_{\odot}$). The latest HST observations of SN 1992A seem to imply complete trapping of the positrons although they also assumes that the V band follows the bolometric light curve.

9.3 Conclusions

We can not say whether positrons escape the ejecta or not, but we can point out that the V band light curve do not follow the bolometric light curve. They deviate from each other more as time goes on. Time dependent bolometric corrections seem to be needed if the V band light curve should be used instead of a bolometric light curve. Because this is the first study of late time photometry in all the optical– and in the near–infrared bands at the same time, further studies should be done to confirm the results we have arrived at here.

The steepening of the V band compared to modelled bolometric light curve could be due to a temperature effect and positron escape is not the only way to explain this feature. Our bolometric light curve has a linear slope, if we take the difference between the first and the last epoch and divide this with the time in days, that shows a faster decline than the expected decline from the cobalt decay.

We need to do more observations in all passbands at late times to see if the behaviour of SN 2000cx at these late phases are the same for other SNe Type Ia. Models are needed to interpret the result we have arrived at here.

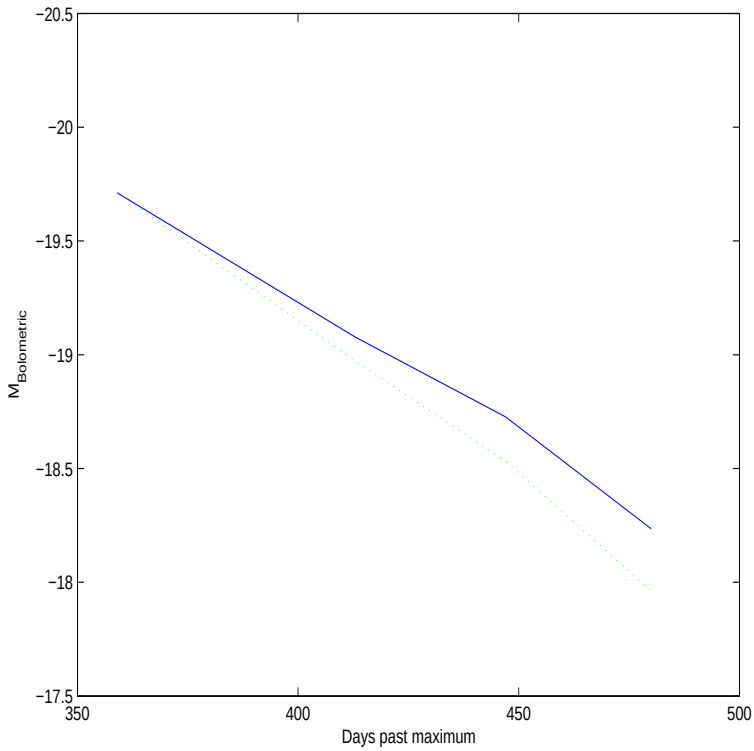

Figure 21: V–band against the bolometric lightcurve
The blue curve is the bolometric light curve and the green dotted one is the V band light curve. We clearly see that the V band light curve do not follow the bolometric light curve.

References

[1] Arnett, W. D., 1969, Astrophys. Space Sci. 5, 168

[2] Bessel, M. S., 1990 PASP, 102, 1181

[3] Candia, P., Krisciunas, K., Suntzeff, N. B., et al., 2003, PASP, 115, 277

[4] Cappellaro, E., Massali, P. A., Benetti, S., et al., 1997, A&A, 328, 203

[5] Casali, M. M., Hawarden, T. G., 1992, UKIRT Newsletter, 4, 33

[6] Chan, K. W., Lingenfelter, R. E., 1993, ApJ, 405, 614

[7] Colgate, S. A., Petschek, A. G.,& Kriese, J. T., 1980, ApJ, 237, 81

[8] Elias, J. H., Frogel, J. A., 1983, ApJ, 268, 718

[9] Filippenko, A. V., 1997, ARA&A, 35, 309

[10] Fitzpatrick, E. L., 1999, PASP, 111, 63

[11] Fransson, C., Houch, J., Kozma, C., 1996, Supernovae and Supernova remnants, eds. McCray R. and Wang Z. Cambridge University Press, Cambridge, p. 211

[12] Hamuy, M., Phillips, M. M., Suntzeff, N. B., et al., 1996, AJ, 112, 2438

[13] Harris, W. E., 1981, PASP, 93, 507

[14] Hillebrandt, W., Niemeyer, J. C., Reinecke, R., 1999, in Cosmic explosion: tenth Astrophysics Conference, College Park, Maryland, 11-13 October 1999, eds. S. Holt, W. Zhang (astro-ph 0005584)

[15] Howell, Steve. B., 2000, Handbook of CCD Astronomy. Cambridge University Press, New York

[16] Höflich, P., Wheeler, J. C., Wang, L., 1999, ApJ, 521, 179

[17] Landolt, A., 1992, AJ, 104, 340

[18] Leibundgut, B., 2000, A&ARv, 10, 179

[19] Li, W. D., Filippenko, A. V., Gates, E., et al., 2001, PASP, 113, 1178

[20] Livio, M., 2001, in Supernovae and Gamma-Ray Bursts: The greatest Explosions since the Big Bang, eds. M. Livio, N. Panagia and K. Sahu Cambridge University Press, 2001, Cambridge, p. 334 (astro-ph 0005344)

[21] Milne, P. A., The, L. S., & Leising, D., 1999, ApJS, 124, 503

[22] Milne, P. A., The, L. S., & Leising, D., 2001, ApJ, 559, 1019

[23] Minkowski, R., 1941, PASP, 53, 224

[24] Niemeyer, J. C., Reinecke M., Hillebrandt W., 2002, arXiv:astro-ph/0203369

[25] Nomoto, K., Thielemann, F–K., Yokoi, K., 1984, ApJ, 286, 644

[26] Persson, S. E., Murphy, D. C., Krzeminski, W., et al., 1998 AJ, 116, 2475

[27] Phillips, M. M., 1993, ApJ, 413, 105

[28] Phillips, M. M., Lira, P., Suntzeff, N. B., et al., 1999, AJ, 118, 1766

[29] Renzini, A., 1996, Supernovae and Supernova remnants, eds. McCray R. and Wang Z. Cambridge University Press, Cambridge, p. 77

[30] Ruiz–Lapuente, P., Spruit, H. C., 1998, ApJ, 500, 360

[31] Shklovskii, I. S., 1978, Stars: Their birth, life, and death., W.H. Freeman and Company, San Francisco

[32] Suntzeff, N. B., 1996, Supernovae and Supernova remnants, eds. McCray R. and Wang Z. Cambridge University Press, Cambridge, p. 41

[33] Tammann, G. A.,1982, Supernovae: A Survey of Current Research, ed. M. J. Rees and R. J. Stoneham (Dordrecht:Reidel), p. 371

[34] Zwicky, F., Baade, W., 1934, PNAS, 20, 254

10 Appendix

Bias and Flat field images

Date	Number of bias images
2001-07-20	5
2001-07-21	5
2001-09-12	5
2001-10-09	10
2001-10-16	7
2001-10-18	10
2001-11-18	5
2001-11-19	10

Table 20: Bias images

Date	Filter	Number of flat field images in each filter
2001-07-20	B, I, R, U, V	4
2001-07-21	V	8
2001-09-12	B, I, R, V	4
2001-10-09	R	8
2001-10-16	B, I, V	4
2001-10-18	R	4
2001-11-18	I, R	4
2001-11-19	B, V	4

Table 21: Flat field images

Observation images

Date UT	Filter	MJD[a]	Exposure s	Airmass[a]	Seeing arcsec
2001 07 21	B	52111.361	2x300	1.314	1.05
2001 07 21	V	52111.370	2x240	1.286	0.98
2001 07 21	R	52111.377	2x240	1.266	0.91
2001 07 21	I	52111.384	2x500	1.249	0.90
2001 07 21	U	52111.398	2x780	1.225	1.05
2001 07 22	V	52112.344	2x300	1.376	0.91
2001 09 13	V	52165.246	3x300	1.231	0.94
2001 09 13	I	52165.259	3x800	1.215	0.86
2001 09 13	B	52165.291	3x400	1.213	0.92
2001 09 13	R	52165.307	4x400	1.233	0.87
2001 10 10	R	52192.135	750+418	1.336	0.93
2001 10 17	I	52199.148	8x650	1.240	0.68
2001 10 17	B	52199.215	4x750	1.235	0.67
2001 10 17	V	52199.253	4x750	1.348	0.86
2001 10 19	R	52201.216	4x750	1.247	0.86
2001 11 19	I	52232.017	8x650	1.375	0.92
2001 11 19	R	52232.083	4x750	1.210	0.78
2001 11 20	V	52233.017	4x750	1.360	0.84
2001 11 20	B	52233.055	4x750	1.240	0.79

Table 22: Optical observations of SN 2000cx.

[a] Refers to the first image of the ObsID

Transformation equation parameters

Date	Filter	Extinction	Colorterm
2001 07 21	U	0.442 (0.015)	0.111 (0.020)
	B	0.212 (0.009)	-0.068 (0.006)
	V	0.112 (0.006)	0.014 (0.003)
	R	0.074 (0.006)	0.016 (0.006)
	I	0.028 (0.007)	-0.045 (0.013)
2001 11 20	B	0.301 (0.008)	-0.085 (0.011)
	V	0.185 (0.006)	0.037 (0.010)
	R	0.130 (0.037)	0.053 (0.035)
	I	0.092 (0.009)	-0.024 (0.030)

Table 23: Colorterms when the extinction coefficients are set to ESO values

Magnitudes for the optical standard stars

Object id	V	error(V)	BV	error(BV)	UB	error(UB)	VR	error(VR)	VI	error(VI)
Mark A	13.258	0.002	-0.245	0.002	-1.203	0.002	-0.119	0.003	-0.253	0.004
Mark A1	15.898	0.007	0.602	0.009	0.016	0.016	0.371	0.009	0.725	0.010
Mark A2	14.536	0.004	0.659	0.005	0.115	0.008	0.372	0.005	0.748	0.005
Mark A3	14.805	0.004	0.947	0.006	0.683	0.014	0.576	0.005	1.105	0.005
PG1323-086	13.478	0.002	-0.128	0.002	-0.672	0.003	-0.047	0.003	-0.105	0.004
PG1323-086A	13.650	0.002	0.395	0.003	0.049	0.004	0.255	0.003	0.503	0.003
PG1323-086B	13.415	0.002	0.768	0.003	0.238	0.005	0.435	0.003	0.842	0.003
PG1323-086C	14.006	0.003	0.714	0.004	0.248	0.007	0.401	0.004	0.772	0.004
PG1323-086D	12.079	0.001	0.591	0.001	0.006	0.003	INDEF	INDEF	INDEF	INDEF
PG2331+055	15.188	0.005	-0.072	0.006	-0.461	0.007	-0.005	0.007	-0.056	0.011
PG2331+055A	13.055	0.002	0.735	0.003	0.205	0.004	0.424	0.002	0.825	0.002
PG2331+055B	14.733	0.004	0.835	0.006	0.407	0.013	0.472	0.005	0.948	0.006
SA109-949	12.836	0.002	0.774	0.003	0.495	0.004	0.500	0.002	1.010	0.002
SA109-954	12.431	0.001	1.308	0.002	0.983	0.005	INDEF	INDEF	INDEF	INDEF
SA109-956	14.643	0.004	1.264	0.006	0.825	0.016	0.744	0.004	1.485	0.005
SA109-949	12.839	0.002	0.788	0.003	0.454	0.004	0.507	0.002	1.005	0.002
SA109-954	12.436	0.001	1.316	0.002	0.939	0.005	INDEF	INDEF	INDEF	INDEF
SA109-956	14.646	0.004	1.268	0.006	0.802	0.018	0.745	0.004	1.478	0.005
SA109-949	12.825	0.002	0.799	0.003	0.416	0.005	INDEF	INDEF	INDEF	INDEF
SA109-954	12.426	0.001	1.319	0.002	0.907	0.006	INDEF	INDEF	INDEF	INDEF
SA109-956	14.639	0.004	1.279	0.007	0.760	0.019	INDEF	INDEF	INDEF	INDEF

Table 24: Magnitudes of the first epoch standard stars

Object id	V	error(V)	BV	error(BV)	VR	error(VR)	VI	error(VI)
PG2213-006	14.124	0.003	-0.217	0.003	-0.079	0.004	-0.196	0.005
PG2213-006A	14.174	0.003	0.666	0.004	0.402	0.003	0.792	0.004
PG2213-006B	12.714	0.001	0.751	0.001	0.424	0.001	0.821	0.001
PG2213-006C	15.096	0.005	0.728	0.006	0.415	0.006	0.842	0.006
Rubin 152	INDEF	INDEF	INDEF	INDEF	INDEF	INDEF	INDEF	INDEF
Rubin 152A	INDEF	INDEF	INDEF	INDEF	INDEF	INDEF	INDEF	INDEF
Rubin 152B	INDEF	INDEF	INDEF	INDEF	INDEF	INDEF	INDEF	INDEF
Rubin 152F	INDEF	INDEF	INDEF	INDEF	INDEF	INDEF	INDEF	INDEF
SA100-267	13.027	0.002	0.485	0.002	INDEF	INDEF	INDEF	INDEF

Table 25: Magnitudes of the last epoch standard stars

Magnitudes of our local optical standard stars

object id	V	error(V)	BV	error(BV)	UB	error(UB)	VR	error(VR)	VI	error(VI)
0720-1	22.059	0.012	1.748	0.048	0.388	0.219	0.976	0.014	2.582	0.013
0720-2	22.460	0.016	0.885	0.036	0.182	0.151	0.620	0.018	1.246	0.021
0720-3	22.337	0.016	1.407	0.043	1.018	0.413	1.047	0.017	2.614	0.017
0720-4	21.409	0.009	1.546	0.025	0.928	0.149	1.001	0.010	2.346	0.010
0720-5	22.522	0.021	0.832	0.038	0.369	0.183	0.482	0.024	1.005	0.029
0720-6	20.845	0.006	0.760	0.010	0.011	0.029	0.525	0.008	1.055	0.008
0720-7	20.123	0.004	0.319	0.005	-1.200	0.009	0.431	0.005	0.690	0.006
0720-8	21.571	0.009	1.562	0.025	1.049	0.192	1.075	0.010	2.692	0.010
0720-9	21.543	0.009	1.549	0.025	1.120	0.203	0.940	0.010	1.983	0.010
0720-10	20.932	0.006	1.100	0.012	0.596	0.057	0.683	0.007	1.328	0.007
0720-11	21.876	0.009	0.821	0.020	0.063	0.066	0.554	0.011	1.102	0.013
0720-12	22.634	0.022	1.687	0.068	3.428	3.215	1.379	0.023	2.590	0.024
0720-13	22.453	0.015	0.809	0.034	-0.852	0.072	0.578	0.018	1.134	0.024
0720-14	20.520	0.005	1.552	0.012	1.114	0.083	1.048	0.005	2.522	0.005
0720-15	21.009	0.006	1.674	0.019	1.107	0.147	1.056	0.007	2.474	0.007
0720-16	21.480	0.008	1.762	0.029	1.066	0.206	1.147	0.009	2.898	0.009
0720-17	23.115	0.026	1.874	0.160	0.599	0.559	1.092	0.028	2.852	0.028
0720-18	21.970	0.012	0.806	0.020	0.282	0.071	0.554	0.014	1.125	0.017
0720-19	21.252	0.007	0.515	0.011	-0.227	0.030	0.376	0.009	0.726	0.010
0720-20	21.656	0.009	1.479	0.029	1.041	0.227	0.913	0.010	1.968	0.010
0720-21	23.564	0.042	1.124	0.094	-0.523	0.243	0.690	0.051	1.190	0.070
0720-22	22.751	0.029	0.926	0.045	0.878	0.293	0.557	0.035	1.191	0.039
0720-23	23.043	0.035	0.880	0.063	0.665	0.288	0.560	0.039	1.170	0.050
0720-24	22.859	0.033	0.687	0.046	0.051	0.114	0.468	0.040	0.988	0.046
0720-25	23.226	0.043	0.886	0.077	0.932	0.455	0.675	0.051	1.589	0.063
0720-26	23.572	0.041	1.094	0.080	-0.418	0.312	0.564	0.047	1.122	0.056
0720-27	23.477	0.039	1.342	0.090	-0.054	0.360	1.093	0.042	2.660	0.043
0720-28	23.184	0.034	1.534	0.098	0.215	0.337	0.738	0.040	1.337	0.045
0720-29	23.181	0.029	0.722	0.046	0.586	0.235	0.640	0.036	1.243	0.040
0720-30	23.116	0.024	0.905	0.057	-0.124	0.228	0.522	0.029	1.186	0.035
0720-31	22.863	0.028	1.604	0.069	-4.253	0.074	1.003	0.029	2.443	0.030
0720-32	22.211	0.013	0.978	0.027	-0.156	0.102	0.579	0.015	1.245	0.016
0720-33	22.801	0.021	0.807	0.046	-0.068	0.141	0.534	0.026	1.060	0.030
0720-34	22.687	0.017	1.076	0.050	-0.624	0.101	0.555	0.020	1.284	0.024
0720-35	22.054	0.013	0.462	0.018	-0.318	0.053	0.359	0.017	0.744	0.021
0720-36	23.434	0.039	1.673	0.120	-0.236	0.501	1.322	0.040	2.991	0.041
0720-37	21.641	0.009	1.313	0.022	1.318	0.184	0.852	0.011	1.699	0.010
0720-38	23.092	0.030	0.635	0.048	0.064	0.146	0.586	0.036	1.144	0.041
0720-39	23.043	0.035	0.880	0.063	0.665	0.288	0.560	0.039	1.170	0.050
0720-40	23.025	0.029	0.751	0.049	-0.093	0.145	0.521	0.034	1.146	0.040
0720-41	22.915	0.025	0.729	0.047	0.152	0.156	0.492	0.034	1.009	0.036
0720-42	23.175	0.028	1.489	0.078	0.660	0.494	1.075	0.031	2.718	0.031
0720-43	22.402	0.016	0.770	0.028	-0.131	0.090	0.492	0.019	1.045	0.024
0720-44	24.084	0.074	1.403	0.200	-0.622	0.508	1.322	0.075	3.036	0.079
0720-45	23.193	0.027	0.620	0.048	-0.026	0.175	0.517	0.034	0.971	0.046
0720-46	22.993	0.028	1.156	0.065	-0.274	0.181	0.953	0.030	1.792	0.034
0720-47	23.468	0.038	1.160	0.101	2.189	1.667	0.744	0.044	1.556	0.047

Table 26: Magnitudes of local standard candidates First epoch

The INDEF values in table 14 means that this stars are saturated and we will not use it when looking for local standard stars.

object id	V	error(V)	BV	error(BV)	VR	error(VR)	VI	error(VI)
1119-1	22.128	0.008	1.584	0.027	1.105	0.009	2.570	0.009
1119-2	22.394	0.009	0.921	0.018	0.508	0.011	1.121	0.013
1119-3	22.308	0.008	1.490	0.026	1.086	0.009	2.506	0.009
1119-4	21.356	0.004	1.583	0.013	0.976	0.005	2.239	0.004
1119-5	22.487	0.010	0.882	0.020	0.433	0.013	0.942	0.016
1119-6	20.809	0.004	0.799	0.006	0.452	0.005	0.993	0.006
1119-7	20.099	0.002	0.332	0.003	0.333	0.003	0.592	0.004
1119-8	21.568	0.005	1.621	0.015	1.094	0.005	2.586	0.005
1119-9	21.534	0.005	1.591	0.014	0.887	0.005	1.896	0.006
1119-10	20.895	0.003	1.103	0.007	0.586	0.003	1.260	0.004
1119-11	21.839	0.006	0.843	0.010	0.471	0.007	1.063	0.009
1119-12	22.586	0.012	1.954	0.056	1.300	0.013	2.477	0.013
1119-13	22.407	0.011	0.809	0.018	0.497	0.013	1.058	0.016
1119-14	20.501	0.002	1.578	0.006	1.063	0.002	2.230	0.002
1119-15	20.962	0.003	1.715	0.010	1.067	0.003	INDEF	INDEF
1119-16	21.465	0.004	1.728	0.015	1.235	0.004	INDEF	INDEF
1119-17	23.197	0.019	1.777	0.081	1.252	0.020	2.807	0.020
1119-18	21.889	0.006	0.852	0.011	0.454	0.007	1.030	0.009
1119-19	21.210	0.004	0.521	0.006	0.280	0.005	0.692	0.006
1119-20	21.661	0.005	1.431	0.013	0.864	0.005	1.907	0.006
1119-21	23.511	0.025	0.942	0.050	0.494	0.036	1.119	0.039
1119-22	22.734	0.016	0.915	0.027	0.531	0.020	1.209	0.022
1119-23	23.003	0.016	0.983	0.031	0.493	0.021	1.128	0.024
1119-24	22.877	0.018	0.754	0.028	0.455	0.026	0.995	0.032
1119-25	23.002	0.027	0.858	0.061	0.422	0.038	1.196	0.057
1119-26	23.616	0.025	0.952	0.051	0.576	0.029	1.179	0.036
1119-27	23.423	0.020	1.810	0.080	1.098	0.021	2.470	0.021
1119-28	23.130	0.022	1.362	0.056	0.719	0.027	1.306	0.033
1119-29	23.104	0.016	0.743	0.029	0.560	0.021	1.125	0.025
1119-30	23.126	0.016	0.885	0.030	0.469	0.021	1.031	0.026
1119-31	22.872	0.012	1.772	0.049	1.066	0.013	2.387	0.013
1119-32	22.190	0.007	0.951	0.015	0.524	0.009	1.167	0.011
1119-33	22.755	0.013	0.761	0.022	0.454	0.015	0.954	0.020
1119-34	22.719	0.011	1.078	0.024	0.570	0.014	1.211	0.016
1119-35	21.993	0.007	0.479	0.010	0.231	0.009	0.602	0.014
1119-36	23.352	0.020	1.820	0.084	1.328	0.020	2.830	0.021
1119-37	21.590	0.005	1.388	0.013	0.771	0.005	1.607	0.006
1119-38	23.087	0.017	0.850	0.034	0.577	0.022	1.150	0.026
1119-39	23.003	0.016	0.983	0.031	0.493	0.021	1.128	0.024
1119-40	22.960	0.014	0.757	0.026	0.419	0.018	0.953	0.022
1119-41	22.906	0.014	0.733	0.025	0.450	0.019	0.987	0.021
1119-42	23.081	0.016	1.501	0.049	1.059	0.017	2.526	0.017
1119-43	22.385	0.010	0.752	0.017	0.441	0.012	0.998	0.015
1119-44	23.910	0.037	1.579	0.108	1.229	0.037	2.792	0.039
1119-45	23.182	0.016	0.752	0.029	0.440	0.022	0.986	0.028
1119-46	22.960	0.014	1.125	0.030	0.875	0.015	1.714	0.017
1119-47	23.453	0.020	1.375	0.067	0.780	0.024	1.526	0.027

Table 27: Magnitudes of local standard candidates Last epoch

Instrumental magnitudes for our local optical standard stars

v0720	v0721	v0912	v1016	v1119
20.65 (0.02)	20.79 (0.02)	20.34 (0.01)	20.20 (0.01)	20.31 (0.01)
18.97 (0.01)	19.07 (0.01)	18.66 (0.01)	18.53 (0.01)	18.64 (0.01)
19.66 (0.01)	19.76 (0.01)	19.35 (0.01)	19.23 (0.01)	19.34 (0.01)
19.05 (0.01)	19.15 (0.01)	18.72 (0.01)	18.63 (0.01)	18.71 (0.01)
20.00 (0.01)	20.10 (0.01)	19.68 (0.01)	19.57 (0.01)	19.67 (0.01)
20.58 (0.01)	20.71 (0.01)	20.26 (0.01)	20.14 (0.01)	20.24 (0.01)
19.38 (0.01)	19.47 (0.01)	19.07 (0.01)	18.96 (0.01)	19.05 (0.01)
19.77 (0.01)	19.87 (0.01)	19.47 (0.01)	19.36 (0.01)	19.47 (0.01)
20.87 (0.03)	21.00 (0.03)	20.55 (0.02)	20.47 (0.01)	20.56 (0.02)
21.17 (0.03)	21.24 (0.03)	20.91 (0.02)	20.74 (0.01)	20.83 (0.02)
20.33 (0.01)	20.44 (0.01)	20.04 (0.01)	19.93 (0.01)	20.01 (0.01)
21.04 (0.03)	21.09 (0.03)	20.68 (0.02)	20.62 (0.01)	20.74 (0.01)
20.53 (0.02)	20.66 (0.02)	20.22 (0.01)	20.11 (0.01)	20.22 (0.01)
21.11 (0.03)	21.18 (0.03)	20.79 (0.02)	20.66 (0.01)	20.78 (0.01)

Table 28: V-band Instrumental magnitudes of local standards

b0720	b0912	b1016	b1119
22.08 (0.04)	21.73 (0.02)	21.68 (0.01)	21.77 (0.02)
20.32 (0.01)	19.99 (0.01)	19.90 (0.01)	20.00 (0.01)
21.86 (0.02)	21.51 (0.02)	21.42 (0.01)	21.58 (0.02)
20.77 (0.01)	20.40 (0.01)	20.34 (0.01)	20.41 (0.01)
21.42 (0.02)	21.07 (0.01)	21.00 (0.01)	21.07 (0.01)
21.98 (0.03)	21.65 (0.02)	21.57 (0.01)	21.61 (0.02)
20.47 (0.01)	20.09 (0.01)	20.02 (0.01)	20.10 (0.01)
21.90 (0.03)	21.51 (0.02)	21.48 (0.01)	21.54 (0.01)
22.40 (0.04)	22.01 (0.03)	22.00 (0.02)	22.05 (0.03)
22.65 (0.06)	22.33 (0.03)	22.24 (0.02)	22.39 (0.03)
21.92 (0.03)	21.49 (0.02)	21.48 (0.01)	21.54 (0.02)
22.36 (0.04)	22.00 (0.03)	21.92 (0.02)	22.02 (0.03)
21.89 (0.03)	21.48 (0.02)	21.45 (0.01)	21.52 (0.02)
22.89 (0.06)	22.47 (0.03)	22.46 (0.02)	22.50 (0.03)

Table 29: B-band Instrumental magnitudes of local standards

i0720	i0912	i1016	i1118
20.33 (0.02)	20.19 (0.01)	20.14 (0.01)	20.22 (0.01)
18.61 (0.01)	18.46 (0.01)	18.42 (0.01)	18.50 (0.01)
18.42 (0.01)	18.29 (0.01)	18.26 (0.01)	18.34 (0.01)
18.43 (0.01)	18.28 (0.01)	18.26 (0.01)	18.32 (0.01)
19.59 (0.01)	19.43 (0.01)	19.40 (0.01)	19.46 (0.01)
20.14 (0.02)	19.98 (0.01)	19.94 (0.01)	20.03 (0.01)
19.33 (0.01)	19.15 (0.01)	19.15 (0.01)	19.19 (0.01)
18.55 (0.01)	18.42 (0.01)	18.39 (0.01)	18.46 (0.01)
20.38 (0.02)	20.18 (0.01)	20.16 (0.01)	20.21 (0.02)
20.69 (0.03)	20.54 (0.01)	20.50 (0.01)	20.56 (0.02)
19.79 (0.01)	19.69 (0.01)	19.65 (0.01)	19.71 (0.01)
20.72 (0.02)	20.57 (0.01)	20.51 (0.01)	20.60 (0.01)
20.17 (0.02)	20.03 (0.01)	20.04 (0.01)	20.07 (0.01)
20.05 (0.02)	19.90 (0.01)	19.87 (0.01)	19.94 (0.01)

Table 30: I-band Instrumental magnitudes of local standards

r0720	r0912	r1009	r1018	r1118
19.94 (0.01)	19.86 (0.01)	20.12 (0.01)	19.90 (0.01)	19.91 (0.01)
18.22 (0.01)	18.19 (0.01)	18.42 (0.01)	18.20 (0.01)	18.22 (0.01)
18.50 (0.01)	18.42 (0.01)	18.67 (0.01)	18.44 (0.01)	18.48 (0.01)
18.15 (0.01)	18.10 (0.01)	18.35 (0.01)	18.12 (0.01)	18.16 (0.01)
19.22 (0.01)	19.18 (0.01)	19.43 (0.01)	19.20 (0.01)	19.23 (0.01)
19.78 (0.01)	19.76 (0.01)	19.99 (0.01)	19.76 (0.01)	19.77 (0.01)
18.78 (0.01)	18.74 (0.01)	18.99 (0.01)	18.76 (0.01)	18.80 (0.01)
18.64 (0.01)	18.57 (0.01)	18.80 (0.01)	18.59 (0.01)	18.63 (0.01)
20.10 (0.02)	20.02 (0.01)	20.27 (0.01)	20.03 (0.01)	20.06 (0.01)
20.39 (0.02)	20.35 (0.01)	20.59 (0.01)	20.32 (0.01)	20.37 (0.02)
19.53 (0.01)	19.48 (0.01)	19.74 (0.01)	19.50 (0.01)	19.52 (0.01)
20.33 (0.01)	20.30 (0.01)	20.49 (0.01)	20.31 (0.01)	20.31 (0.01)
19.81 (0.01)	19.79 (0.01)	20.00 (0.01)	19.77 (0.01)	19.80 (0.01)
19.94 (0.01)	19.91 (0.01)	20.11 (0.01)	19.91 (0.01)	19.92 (0.01)

Table 31: R-band Instrumental magnitudes of local standards

u0720
25.50 (0.02)
23.44 (0.02)
25.91 (0.02)
24.38 (0.05)
24.57 (0.06)
24.32 (0.06)
23.39 (0.03)
25.88 (0.02)
26.28 (0.03)
26.33 (0.03)
24.87 (0.01)
25.60 (0.01)
24.88 (0.01)
25.73 (0.01)

Table 32: U-band Instrumental magnitudes of local standards

Aperture corrections with different sets of stars

Date	Filter	Magnitude	Error in magnitude
0720	U	-0.242	0.015
0720	B	-0.215	0.012
0720	V	-0.186	0.009
0720	R	-0.170	0.008
0720	I	-0.163	0.007

Table 33: Aperture correction with one star

Date	Filter	Magnitude	Error in magnitude
0720	U	-0.260	0.014
0720	B	-0.202	0.011
0720	V	-0.156	0.008
0720	R	-0.136	0.007
0720	I	-0.109	0.006

Table 34: Aperture correction with 47 stars

Date	Filter	Magnitude	Error in magnitude
0720	U	-0.333	0.018
0720	B	-0.291	0.014
0720	V	-0.212	0.010
0720	R	-0.171	0.008
0720	I	-0.148	0.007

Table 35: Aperture correction with 14 stars

Date	Filter	Magnitude	Error in magnitude
1119	B	-0.195	0.009
1119	V	-0.171	0.008
1119	R	-0.232	0.010
1119	I	-0.210	0.009

Table 36: Aperture correction with one star

Date	Filter	Magnitude	Error in magnitude
1119	B	-0.149	0.008
1119	V	-0.127	0.006
1119	R	-0.133	0.007
1119	I	-0.096	0.005

Table 37: Aperture correction with 47 stars

Date	Filter	Magnitude	Error in magnitude
1119	B	-0.205	0.010
1119	V	-0.179	0.008
1119	R	-0.198	0.009
1119	I	-0.153	0.007

Table 38: Aperture correction with 14 stars

Observations in infrared

Date	Filter	Exposure	Airmass	Seeing
2001–07–30	J	13x30	1.23	0.61
2001–07–30	H	13x15	1.21	0.40
2001–07–30	K_s	16x12	1.20	0.39
2001–09–20	J	28x30	1.21	0.49
2001–09–20	H	27x15	1.24	0.40
2001–11–18	J	28x30	1.32	0.63
2001–11–18	H	27x15	1.23	0.48
2001–11–19	J	28x30	1.33	0.60
2001–11–19	H	27x15	1.23	0.44
2001–11–21	J	28x30	1.32	1.00
2001–11–21	H	27x15	1.22	0.68

Table 39: Object Images in the Infrared

Instrumental magnitudes Local standards in IR

Date	j	h	k_s
0730	18.17 (0.01)	17.83 (0.01)	18.07 (0.01)
	20.28 (0.03)	19.56 (0.03)	19.27 (0.03)
	18.52 (0.01)	18.21 (0.01)	18.49 (0.02)
	19.94 (0.02)	19.43 (0.02)	19.69 (0.04)
	18.36 (0.01)	18.02 (0.01)	18.22 (0.02)
	16.16 (0.01)	15.80 (0.01)	16.06 (0.01)
	17.61 (0.01)	17.49 (0.01)	17.94 (0.01)
	19.09 (0.01)	18.67 (0.02)	19.03 (0.02)
	20.42 (0.03)	20.06 (0.04)	20.47 (0.06)
	18.85 (0.01)	18.50 (0.02)	18.79 (0.02)
	21.21 (0.05)	20.86 (0.07)	20.99 (0.09)
	21.02 (0.04)	20.85 (0.07)	21.16 (0.10)
	20.43 (0.03)	20.06 (0.04)	20.43 (0.06)
	20.07 (0.02)	19.39 (0.03)	19.06 (0.02)

Table 40: IR instrumental magnitudes of local standards 0730

Date	j	h
0920	18.23 (0.01)	17.90 (0.01)
	20.31 (0.03)	19.64 (0.03)
	18.56 (0.01)	18.29 (0.01)
	19.98 (0.02)	19.55 (0.02)
	18.40 (0.01)	18.10 (0.01)
	16.20 (0.01)	15.86 (0.01)
	17.65 (0.01)	17.58 (0.01)
	19.14 (0.01)	18.74 (0.01)
	20.46 (0.03)	20.23 (0.04)
	18.89 (0.01)	18.56 (0.02)
	21.25 (0.04)	20.88 (0.06)
	21.05 (0.04)	20.81 (0.05)
	20.45 (0.03)	20.04 (0.03)
	20.10 (0.02)	19.45 (0.03)

Table 41: IR instrumental magnitudes of local standards 0920

Date	j	h
1118	18.22 (0.01)	17.91 (0.01)
	20.34 (0.03)	19.73 (0.03)
	18.57 (0.01)	18.28 (0.01)
	19.97 (0.02)	19.50 (0.03)
	18.40 (0.01)	18.08 (0.01)
	16.18 (0.01)	15.83 (0.01)
	17.65 (0.01)	17.55 (0.01)
	19.13 (0.01)	18.74 (0.02)
	20.52 (0.03)	20.17 (0.04)
	18.88 (0.01)	18.56 (0.02)
	21.21 (0.05)	20.87 (0.01)
	21.06 (0.05)	20.76 (0.07)
	20.45 (0.03)	20.14 (0.04)
	20.10 (0.02)	19.47 (0.03)

Table 42: IR instrumental magnitudes of local standards 1118

Date	j	h
1119	18.17 (0.01)	17.87 (0.01)
	20.30 (0.03)	19.59 (0.03)
	18.53 (0.01)	18.23 (0.01)
	19.92 (0.03)	19.46 (0.03)
	18.36 (0.01)	18.06 (0.01)
	16.14 (0.01)	15.80 (0.01)
	17.61 (0.01)	17.51 (0.01)
	19.08 (0.02)	18.70 (0.02)
	20.42 (0.03)	20.05 (0.04)
	18.86 (0.01)	18.53 (0.02)
	21.22 (0.05)	20.91 (0.08)
	21.02 (0.05)	20.87 (0.08)
	20.42 (0.03)	20.08 (0.04)
	20.09 (0.02)	19.43 (0.03)

Table 43: IR instrumental magnitudes of local standards 1119

Date	j	h
1121	18.46 (0.01)	18.02 (0.01)
	20.62 (0.03)	19.78 (0.03)
	18.80 (0.01)	18.36 (0.01)
	20.22 (0.03)	19.62 (0.03)
	18.63 (0.01)	18.19 (0.01)
	16.40 (0.01)	15.94 (0.01)
	17.87 (0.01)	17.66 (0.01)
	19.40 (0.02)	18.86 (0.02)
	20.71 (0.04)	20.40 (0.05)
	19.14 (0.01)	18.69 (0.02)
	21.43 (0.06)	20.93 (0.07)
	21.23 (0.05)	20.99 (0.07)
	20.76 (0.04)	20.24 (0.04)
	20.38 (0.03)	19.60 (0.03)

Table 44: IR instrumental magnitudes of local standards 1121